ANALYSIS, DESIGN, AND OPERATION OF A SPHERICAL INVERTED-F ANTENNA

A Thesis

by

JACOB JEREMIAH MCDONALD

Submitted to the Office of Graduate Studies of
Texas A&M University
in partial fulfillment of the requirements for the degree of

MASTER OF SCIENCE

May 2009

Major Subject: Electrical Engineering

ANALYSIS, DESIGN, AND OPERATION OF A SPHERICAL INVERTED-F ANTENNA

A Thesis

by

JACOB JEREMIAH MCDONALD

Submitted to the Office of Graduate Studies of
Texas A&M University
in partial fulfillment of the requirements for the degree of

MASTER OF SCIENCE

Approved by:

Chair of Committee,	Gregory Huff
Committee Members,	Ray James
	Robert Nevels
	Steve Wright
Head of Department,	Costas Georghiades

May 2009

Major Subject: Electrical Engineering

ABSTRACT

Analysis, Design, and Operation of a Spherical Inverted-F Antenna. (May 2009)

Jacob Jeremiah McDonald, B.S., Texas A&M University

Chair of Advisory Committee: Dr. Gregory Huff

This thesis presents the analysis, design, and fabrication of a spherical inverted-F antenna (*SIFA*). The *SIFA* consists of a spherically conformal rectangular patch antenna recessed into a quarter section of a metallic sphere. The sphere acts as a ground plane, and a metal strip shorts the patch to the metallic sphere. The *SIFA* incorporates planar microstrip design into a conformal spherical geometry to better meet the design constraints for integrated wireless sensors. The *SIFA* extends a well-established technology into a new application space, including microsatellites, mobile sensor networks, and wireless biomedical implants.

The complete *SIFA* design depends on several parameters, several of which parallel planar design variables. A modified transmission line model determines the antenna input impedance based on the sphere's inner and outer radii, the patch length and width, short length and width, and feed position. The *SIFA* can be tuned to the desired frequency band by choosing the proper outer radius, after which the antenna can be matched by tuning the short characteristics, patch dimensions, and feed position.

The fabricated design was chosen to operate at the MICS band (402-405 MHz), a popular band for biomedically implanted devices. An initial design was constructed with

Styrofoam ($\varepsilon_r \approx 1$) and copper tape. Simulation in HFSS corroborates that *SIFA* operation incorporates the MICS band, with resonant frequency of 404 MHz and 32 MHz (7.9%) bandwidth. The fabricated prototype performs similarly, with a resonant frequency of 407 MHz and 19 (4.7%) MHz bandwidth. Following fabrication, several modifications were implemented to miniaturize the *SIFA* and introduce additional functionality. Slot loading and dielectric coating were implemented to achieve *SIFA* miniaturization. Multiple elements were also introduced to achieve dual band operation and beam steering. A miniaturized *SIFA* was investigated in several biological media, and a lossy coating implemented to maintain impedance match in several different media, with the goal of retaining a matched impedance bandwidth in the MICS band.

NOMENCLATURE

SIFA	Spherical Inverted-F Antenna
PIFA	Planar Inverted-F Antenna
VSWR	Voltage Standing Wave Ratio
IC	Integrated Circuit
MANET	Mobile Ad Hoc Network
PEC	Perfect Electrical Conductor
PMC	Perfect Magnetic Conductor
E-field	Electric Field
H-field	Magnetic Field
E-plane	Plane containing the E-field vector and direction of maximum radiation
H-plane	Plane containing the H-field vector and direction of maximum radiation
TE	Transverse Electric
TM	Transverse Magnetic
G	Antenna Gain
Q	Antenna Q Factor

TABLE OF CONTENTS

LIST OF FIGURES

FIGURE Page

FIGURE Page

LIST OF TABLES

CHAPTER I

INTRODUCTION

The use of wireless systems has expanded to encompass numerous aspects of everyday life since Marconi's pioneering experiments in wireless telegraphy over a century ago [1]. Wireless technology has enabled a broad array of products and services spanning industrial, civilian, military, and healthcare applications. At the consumer level, cell phones and handheld devices have made mobile communication and instant accessibility a necessity [2-3]. Military applications have pushed the envelope even further, with advanced radar and wireless control systems providing the armed forces with information and force superiority (e.g., network-centric warfare, global information grid, precision bombing [4-8]). Similarly, industrial applications utilize wireless sensor technologies to monitor chemical, energy, and manufacturing processes with an ease and precision previously unseen [9-13].

Sensor systems have developed hand-in-hand with wireless technology. A few decades ago, sensor applications were limited to a few minor measurements, such as pressure and temperature monitoring [14-17]. Improvements in integrated circuit (IC) fabrication technologies, combined with microfluidics and chemical analysis, have expanded sensing capabilities to an impressive range of physical data. IC sensor applications now range from particulate concentration measurement and identification to range from particulate concentration measurement and identification to DNA detection

---

This thesis follows the style of *IEEE Transactions on Antennas and Propagation*.

and sequencing [18-19]. As a result, people can monitor and respond to their environment in ways never before imagined. While advancements in micro-fabrication and electronics enable smaller, more efficient sensor systems, wireless applications continue to expand. Combining these technologies promises to achieve instantaneous monitoring of environmental data from anywhere in the world.

With sensor applications multiplying daily, the need arises for integrated wireless systems which are portable, rugged, low-cost and reusable or replaceable. Such systems must effectively package antennas in a host structure that also provides structural housing for various sensor elements and power harvesting devices. For many wireless systems, integrating planar patch antennas onto the surface of existing devices provides an effective solution. For example, planar antennas have been integrated into computers to provide wireless networking [20]. Despite the ease of this approach, planar integration faces difficulties when the sensor position or orientation remains unknown (i.e. mobile, randomly oriented sensors).

A spherical host structure offers a robust solution to mobile, orientation-independent situations by providing maximum real estate for both external radiating elements and electronic sensor systems embedded in the spherical volume. The spherical geometry is highly mobile and aerodynamic, making it a promising candidate for ingested biomedical devices, microsatellite systems, and mobile ad hoc networks (MANETs). The spherical geometry improves antenna visibility in the direction of back radiation, in contrast to planar microstrip antenna technologies, where a larger ground plane can limit radiation to just one hemisphere. The sphere also provides a better

surface for multiple antenna and array configurations, since elements maintain visibility over a larger scan angle. Thus, conforming an antenna to a spherical geometry will both improve wireless performance and sensor functionality. The *SIFA* exploits these advantages to provide a novel, integrated wireless sensor for use in mobile and random orientation applications.

Many packaged antennas use the host structure to contribute to or even enhance the antenna's radiation [21-22]. The Spherical Inverted-F Antenna, or *SIFA*, continues this trend by using the spherical support structure as a ground plane. *SIFA* design parallels planar microstrip techniques and uses well-established design guidelines; however, the *SIFA* requires adaptation to account for additional packaging requirements. As a result, the *SIFA* addresses both electromagnetic and structural design issues. The antenna, although integrated into the sensing structure, remains isolated from internal electronics and sensors, and the recessed antenna structure creates a smooth external geometry. Designing for both the physical and electrical constraints allows the *SIFA* to radiate effectively while maintaining the necessary geometry for small, easily deployable wireless sensors.

This thesis begins with a review of relevant topics in antenna theory to provide a foundational analysis of *SIFA* design techniques. The design and analysis of the *SIFA* follows, with an emphasis on modeling techniques that highlight the relationship between its physical structure and electrical performance; this includes an adaptation of the transmission line model to the spherical geometry. The transmission line model parallels planar microstrip design techniques and provide a comprehensive design

procedure. A parameter study then reveals how various design variables affect antenna performance to provide a qualitative guide to *SIFA* design. *SIFA* fabrication and measurement follow the parameter study to validate the analysis and design process. A discussion of several modifications, including slot loading, dielectric coating, and multiple antenna techniques, focuses on additional benefits and provides operational insight. The thesis concludes with a summary of work accomplished and areas for further research.

CHAPTER II

BACKGROUND

A. Antenna Performance Metrics

A review of antenna performance metrics provides a baseline for comparison between various designs. Fig. 1 provides a general schematic of a transmission line connected to a radiating antenna.

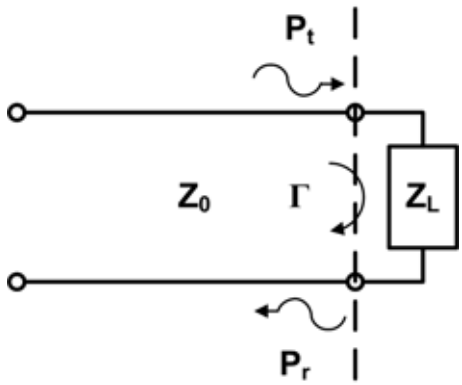

Fig. 1. Antenna Matching. Generic load/antenna with impedance Z_L attached to a transmission line with characteristic impedance Z_0

Forward and backward propagating waves carry power and information down the line. The transmission line has impedance Z_0, and the antenna presents an impedance Z_L, which depends on the antenna geometry and frequency of operation. The reflection coefficient Γ, defined as the ratio of voltage reflected to voltage transmitted, can be found mathematically as [23-25]:

$$\Gamma = \frac{Z_L - Z_0}{Z_L + Z_0} \tag{1}$$

For complete power transmission, $\Gamma = 0$ and $Z_L = Z_0$. Thus, antenna design requires that the antenna impedance matches the line impedance, amongst other design constraints. For the purposes of this work, the characteristic line impedance is 50 Ω. The power reflected can also be measured with the voltage standing wave ratio, or VSWR:

$$VSWR = \frac{1-|\Gamma|}{1+|\Gamma|} \tag{2}$$

Thus, a VSWR = 1 corresponds to a matched antenna. The VSWR is commonly plotted against frequency to illustrate antenna performance, with the VSWR 2:1 bandwidth calculated as the difference between the two frequencies at which the VSWR < 2 (a metric chosen to represent an acceptable impedance match). Since VSWR only provides power information, another metric, the Smith Chart, illustrates the antenna's impedance. A labeled Smith chart with a matched antenna response can be seen in Fig. 2. The horizontal axis corresponds to the real component of Γ, and the vertical axis the imaginary component of Γ. The two sets of intersecting circles indicate the antenna impedance normalized to the characteristic line impedance [23-25]. The dashed circles correspond to the real component of impedance, and the dotted circles correspond to the imaginary component. VSWR and Smith Chart metrics do not indicate whether the antenna dissipates or radiates the input power. Radiation patterns map the radiated power density (W/m^2) over three dimensional space and indicate how much power the antenna radiates in each direction. Radiation patterns depend on the antenna geometry, which determines the field distribution on the structure and thus the radiated field.

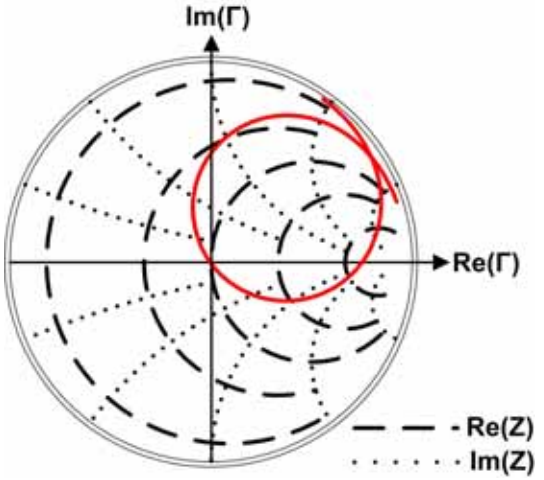

Fig. 2. Smith Chart. Impedance curve (red) plotted on the Smith chart for a matched antenna. The dashed lines are circles of constant resistance and the dotted lines are circles of constant reactance

A general performance metric for antenna size is the factor *ka*, where *k* is the propagation constant and *a* is the radius of a sphere that encloses the entire antenna geometry. Physical limitations on antenna bandwidth and gain occur for electrically small antennas, which can be generally classified as $ka < 1$. Considering free space as a spherical waveguide, the antenna couples radiation into spherical modes which comprise the radiated fields. For $ka < 1$, the antenna size becomes too small to efficiently couple into these propagating modes, in a similar manner to a waveguide operating below cutoff frequency. As a result, the antenna couples into evanescent modes which increase the antenna *Q* and decrease bandwidth. Furthermore, the evanescent modes tend to be omni-directional, limiting the antenna gain. Closed-form expressions for the Q and gain of electrically small antennas, which have been derived in [26-27], can be seen in (3). These limitations explain many of the changes in antenna performance during the *SIFA* miniaturization process.

$$Q = \frac{1 + 3k^2 r^2}{k^3 r^3 \left[1 + k^2 r^2\right]} \qquad (3)$$
$$G = 1.5$$

B. Microstrip Antennas

SIFA analysis and design adapts several microstrip concepts and models to the spherical geometry. Reviewing the physical and analytical models for planar microstrip antennas provides a better understanding of *SIFA* operation. Fig. 3 illustrates the physical geometry of a typical microstrip patch antenna.

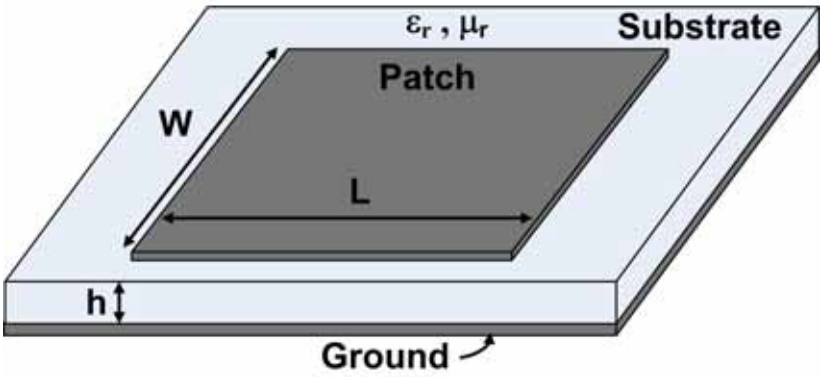

Fig. 3. Patch Antenna - Physical Model. Patch antenna with length *L* and width *W* on a substrate with height *h* and constitutive parameters ε_r and μ_r

The antenna consists of a rectangular conducting patch placed over a conducting ground plane, with a dielectric substrate in between. The antenna can be fed via several methods, including coaxial probe excitation, aperture coupling, or microstrip line feeding. For the purpose of *SIFA* design, the probe-fed rectangular patch antenna will be

most relevant, although the models outlined in this section apply to other patch geometries and excitation methods as well.

The transmission line and cavity models provide a baseline for comparison to the electrical performance of the *SIFA*. In order to better understand the transmission line model, the cavity model will be discussed first. The cavity model treats the patch as a cavity with electric walls (PEC) on top and bottom and magnetic walls (PMC) on the sides, as illustrated in Fig. 4 [28-31]. The cavity model assumes a thin substrate ($h/\lambda < 1/10$). The boundary conditions in Fig. 4 seem to prevent any radiation from the fields inside the cavity, since the walls present a purely reactive impedance. The radiated fields can be determined, however, according to magnetic currents derived from Huygen's principle [32].

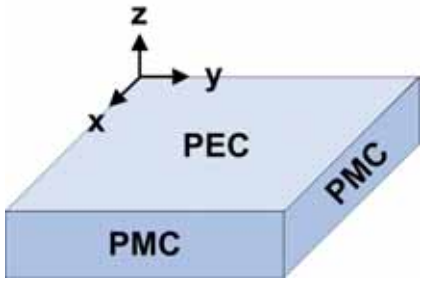

Fig. 4. Cavity Model - Boundary Conditions. Electromagnetic boundary conditions of the microstrip patch antenna according to the cavity model

Based on these boundary conditions, the fields inside the cavity can be solved according to classical techniques in electromagnetics [23]. Eq. (4) provides expressions for the fields inside the cavity for the fundamental TM_{10} mode, which occurs at the antenna's lowest resonant frequency.

$$E_z = E_0 \cos\left(\frac{\pi}{L} y\right)$$
$$H_x = H_0 \sin\left(\frac{\pi}{L} y\right) \tag{4}$$
$$E_x = E_y = H_y = H_z = 0$$

The typical patch length $L = \lambda/2$ results in (4). Fig. 5 depicts the field structure of the TM_{10} mode, which has a sinusoidal variation in the patch length (y), and uniform field structure across the patch width (x) and patch height (z). The electric field maximum occurs at the patch edge, and the minimum occurs at the patch center. Radiation occurs according to Huygen's principle [32], which allows the fields tangential to an aperture to be modeled by an equivalent magnetic or electric current. For the case of the patch, the tangential electric fields at the sides of the patch, also known as "slots", can be modeled as magnetic currents according to (5).

$$\vec{M} = -2\hat{n} \times \vec{E} \tag{5}$$

Based on the field distribution inside the cavity, the magnetic currents are found as in Fig. 6.

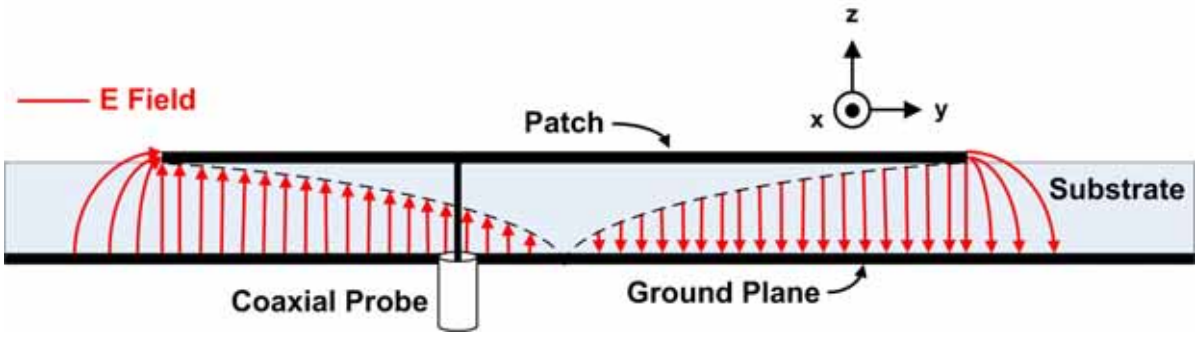

Fig. 5. Patch Antenna - Field Distribution. Electric field distribution for the TM_{10} mode

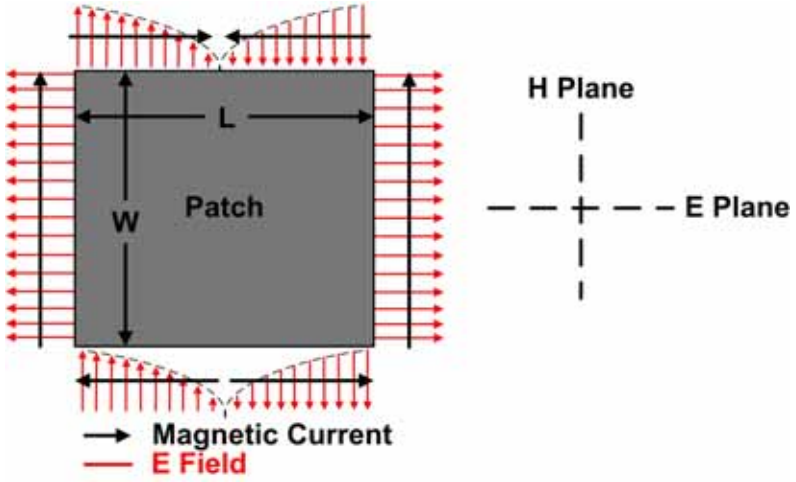

Fig. 6. Patch Antenna - Equivalent Magnetic Currents. Equivalent magnetic currents for the TM_{10} mode according to Huygen's Principle. The side slots, separated by the patch width *W*, contribute little radiation due to the reversal of magnetic current within the slot

The two slots separated by the patch length act as a two element array to provide the primary radiation. The side slots contribute little radiation. The reversal of magnetic current direction within the slot cancels the fields in the H-plane, and the phase reversal between slots cancels the fields out in the E-plane. The resulting radiated fields for the TM_{10} mode can be seen in Fig. 7.

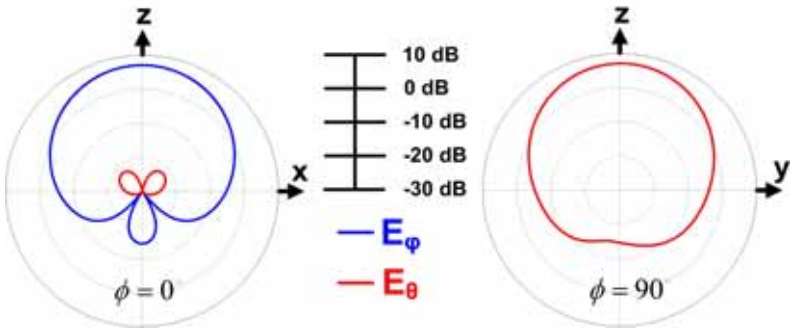

Fig. 7. Patch Antenna - Radiated Fields. Radiated fields of the planar microstrip patch antenna in the two primary cut planes. The fields were determined from numerical simulation in HFSS

These fields match well with those produced by a *λ/2* spaced array of two slots. The cross-polarization produced by the side slots (E_θ in the $\varphi = 0°$ plane and E_φ in the $\varphi = 90°$ plane) remains at least 20 dB below the primary radiation, which verifies the null effect of the side slots.

The cavity model provides physical insight into the field structure and radiation mechanism of the microstrip patch antenna. The transmission line model maps the field structure and radiation mechanism into an equivalent circuit [33-36]. By considering the patch as a low impedance transmission line and determining the admittance of the radiating slots, a circuit model can be derived which accurately predicts the patch input impedance and resonant frequency. The transmission line model for the patch antenna can be seen in Fig. 8.

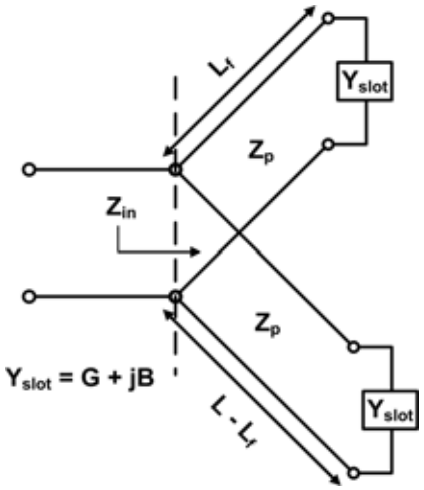

Fig. 8. Patch Antenna - Transmission Line Model. Transmission Line model for the microstrip patch antenna with patch length *L*, characteristic impedance Z_p, feed position L_f, and slot admittance Y_{slot}

The two radiating slots have admittance $Y = G+jB$, where the conductance G corresponds to the radiated field, and the susceptance B results from the non-radiating fringing field. Closed form expressions for the slot conductance and susceptance have been derived as [23,37]:

$$G = \frac{W}{120\lambda_0}\left[1-\frac{1}{24}\left(k_0 h\right)^2\right], \frac{h}{\lambda_0} < \frac{1}{10}$$
$$B = \frac{W}{120\lambda_0}\left[1-0.636\ln\left(k_0 h\right)\right], \frac{h}{\lambda_0} < \frac{1}{10} \quad (6)$$

where h is the substrate thickness and k_0 the wave number. These expressions assume a thin substrate in keeping with the cavity model, but expressions for thicker slots are available [37]. The patch characteristic impedance Z_p can be calculated according to standard analysis formulas, given in (7) [25, 37].

$$w = \frac{c}{2f_r}\sqrt{\frac{2}{\varepsilon_r+1}}$$
$$\varepsilon_{eff} = \frac{\varepsilon_r+1}{2}+\frac{\varepsilon_r-1}{2}\left(1+\frac{12h}{w}\right)^{\frac{-1}{2}} \quad (7)$$
$$Z_0 = \frac{\left[120\pi\left(\varepsilon_{eff}\right)^{\frac{-1}{2}}\right]}{\left(w/h\right)+1.393+0.667\ln\left(1.444+w/h\right)}, w/h \geq 1$$

Based on the choice of substrate permittivity, substrate thickness, and patch width, the slot and transmission line characteristics can be determined. The choice of substrate

material (or permittivity) impacts antenna size and bandwidth, with higher permittivities corresponding to smaller antennas with lower bandwidth. In a similar manner, thinner substrates result in lower bandwidth. Once these selections have been made, the feed location determines the antenna input impedance. The separation between each slot and the feed depends on the patch length L and feed position L_f. The patch length $L = \lambda/2$ according to the cavity model, although a slight modification accounts for an effective length extension due to fringing fields and mutual coupling between the slots. These modifications give [23]:

$$L = \frac{c}{2f_r\sqrt{\varepsilon_{eff}}} - 2\Delta L$$
$$\Delta L = 0.412h\frac{\left(\varepsilon_{eff}+0.3\right)\left(\frac{w}{h}+0.264\right)}{\left(\varepsilon_{eff}-0.258\right)\left(\frac{w}{h}+0.8\right)} \quad (8)$$

The effective length extension ΔL depends on the substrate thickness, patch width, and substrate permittivity. With the patch length determined by the desired resonant frequency, the probe position determines the input impedance, which depends on the ratio of electric to magnetic field (E/H) at the feed location. Consequently, the feed should be placed with a consideration to the field structure. Based on the fields for the TM_{10} mode from (4), the electric field is a maximum at the patch edge and a minimum at the patch center, and the magnetic field is a minimum at the patch edge and a maximum at the center. As a result, the input impedance becomes largest at the patch edge and drops to zero at the patch center. An exact expression for the feed position required to

achieve the desired input impedance R_{in} can be found in (9), where $R_{in,0}$ is the impedance at the patch edge. Based on the models outlined above, the substrate material, substrate thickness, patch width, length, and feed position can be chosen to achieve the desired resonant frequency and input impedance. The transmission line model provides a reference for analytical models used in *SIFA* design.

$$R_{in} = R_{in,0} \cos^2\left(\frac{\pi}{L} L_f\right) \tag{9}$$

C. Antenna Miniaturization Techniques

Microstrip antenna miniaturization has traditionally focused on three methods: dielectric loading, slot loading, and shorting techniques. The *SIFA* miniaturization process first implemented shorting, followed by slot loading and dielectric coating. Each technique will be discussed in the order of implementation in the *SIFA*. The shorting concept originated in low-profile linear antennas [38], but quickly found application in microstrip antennas as well**.** Microstrip antennas utilizing shorting techniques have become known as Planar Inverted-F Antennas [39-41], which can also refer to a specific design which utilizes a shorting plane at the patch center. Based on the electric field symmetry in the traditional microstrip patch, a shorting wall can be inserted at the patch center (i.e. the electric field minimum) without affecting the TM_{10} mode of patch operation [42]. The resulting structure has been labeled the Planar Inverted-F Antenna, or *PIFA*, because the antenna profile resembles the letter F, as can be seen in Fig. 9.

Since the *PIFA* maintains the resonant frequency of the original patch at half the size, it can be considered a resonant λ/4 antenna [42]. The *PIFA* can be modeled according to the modified cavity and transmission line model (Figs. 10,11) to account for the shorting wall and the equivalent magnetic currents shown in Fig. 11.

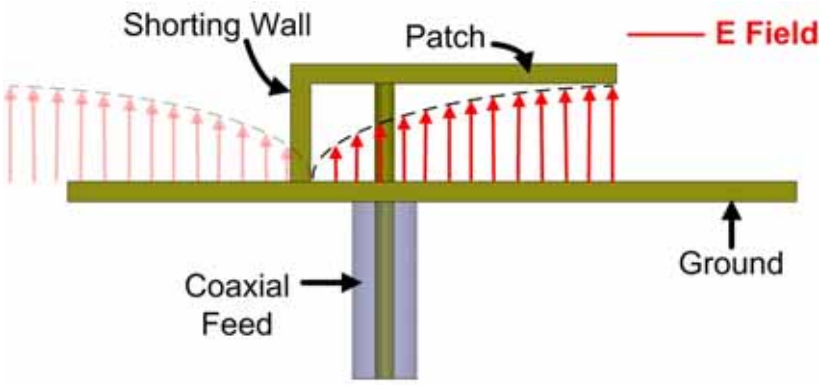

Fig. 9. *PIFA* - Field Distribution. Profile view of the *PIFA*, including the electric field distribution, which corresponds to the TM_{10} mode in the original patch antenna

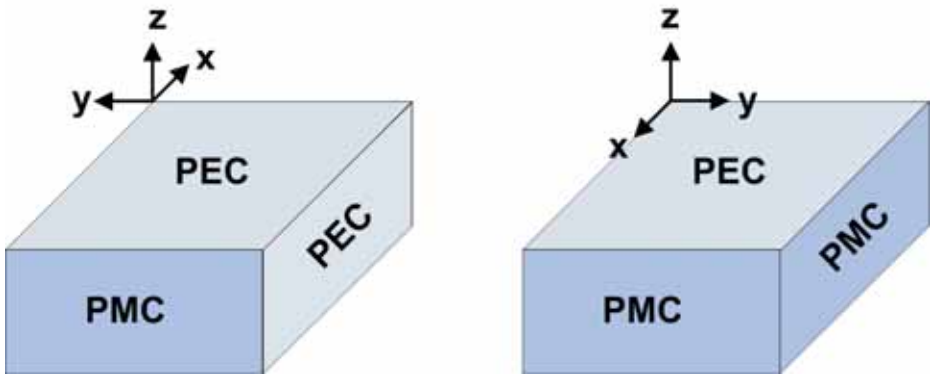

Fig. 10. *PIFA* - Boundary Conditions. Electromagnetic boundary conditions of the *PIFA* according to the cavity model

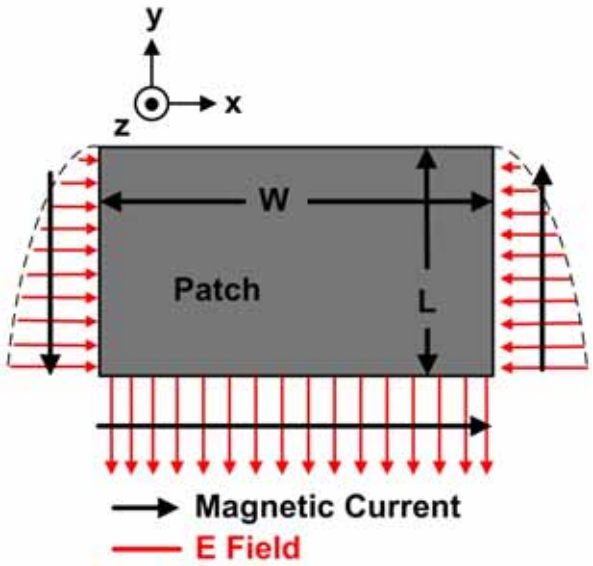

Fig. 11. *PIFA* - Equivalent Magnetic Currents. *PIFA* equivalent magnetic currents according to Huygen's Principle. The equivalent magnetic currents determine the radiated fields

Adjustments must be made to the transmission line model as a result of changes in the equivalent magnetic currents. The effect of the side slots can no longer be neglected. In the original microstrip patch antenna, the reversal of magnetic current in the side slots (see Fig. 6) allowed their removal from the model. The equivalent magnetic current due to the *PIFA* electric field, however, no longer reverses direction, as illustrated in Fig. 11. Fig. 12 provides a transmission line model for the *PIFA*, which is similar to that of the original patch, with the short replacing one of the radiating slots and the side slot admittances added in parallel to the original model. In terms of antenna performance, the side slot radiation increases the loss and thus the antenna bandwidth. The cross polarization also increases because the side slots are oriented perpendicular to the primary radiating slot. The original cavity model was validated by the low cross-polarization in the radiated fields, as evidenced by Fig. 7. Fig. 13 reveals a significant

increase in cross-polarization (E_θ in the $\varphi = 0°$ plane) due to the side slots and validates their consideration in the *PIFA* transmission line model. Cross-polarization remains low in the $\varphi = 90°$ plane, which is equidistant from the two side slots. Modifications in the *PIFA* model due to the shorting wall and resultant changes in equivalent magnetic currents provide a framework for analyzing the shorting mechanism in the *SIFA*. The *PIFA* effectively halves the patch size (from $\lambda/2$ to $\lambda/4$) while retaining similar performance to that of the original patch antenna. Slot loading further reduces patch size by increasing the electrical length of the microstrip patch, requiring the current to flow across a longer path. Fig. 14 illustrates the increase in current path relative to a traditional microstrip patch antenna.

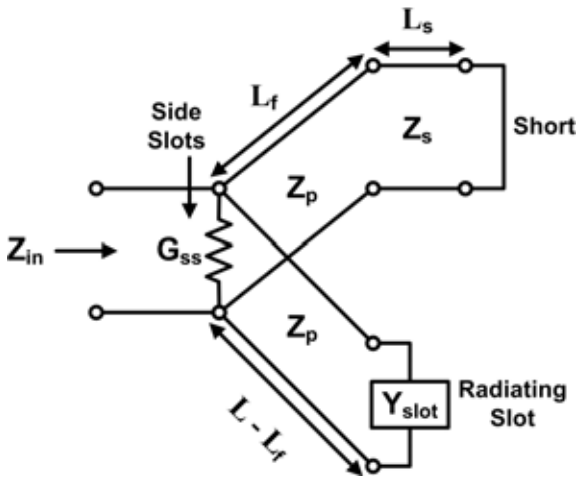

Fig. 12. *PIFA* - Transmission Line Model. Equivalent TL model for the *PIFA* with length *L*, feed position L_f, short length L_s, patch characteristic impedance Z_p, short characteristic impedance Z_s, slot admittance Y_{slot}, and side slot conductance G_{ss}

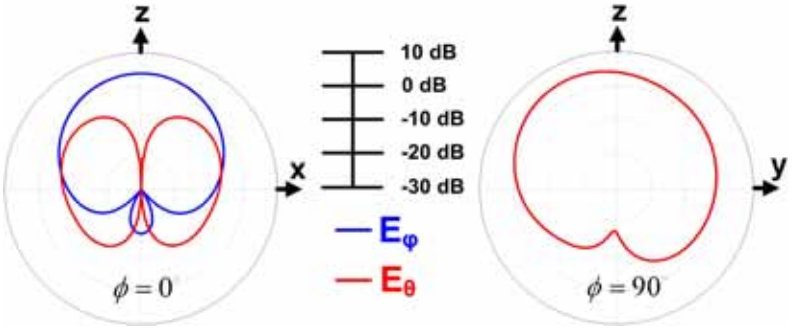

Fig. 13. *PIFA* - Radiated Fields. *PIFA* radiated fields in the primary cut planes. Cross-polarization in the φ = 0° plane increases significantly relative to the patch antenna due to side slot radiation

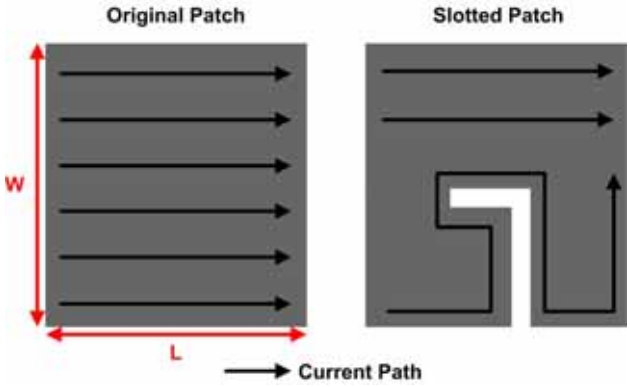

Fig. 14. Comparison of Conventional and Slotted Patches

Slot loading has been implemented with three primary techniques: U-shaped slots in the patch center, linear slots cut into the side of the patch, and L-shaped slots in the side of the patch. Fig 15 presents the patch geometry for each technique. U slot loading traditionally achieves dual band and broadband operation [43-46], but L slot loading provides a larger reduction in operating frequency or size [47]. Further slot loading has resulted in the advent of meander and serpentine microstrip antennas, which have achieved the greatest miniaturization to date [48-49]. Since radiation occurs

primarily from the two slots across the patch length, linear and L-shaped slots have been traditionally implemented in the patch side (i.e. across the patch width) [47, 50-52]. Due to their simplicity and effectiveness in reducing patch size, the linear and L slot geometries will be implemented in the *SIFA*.

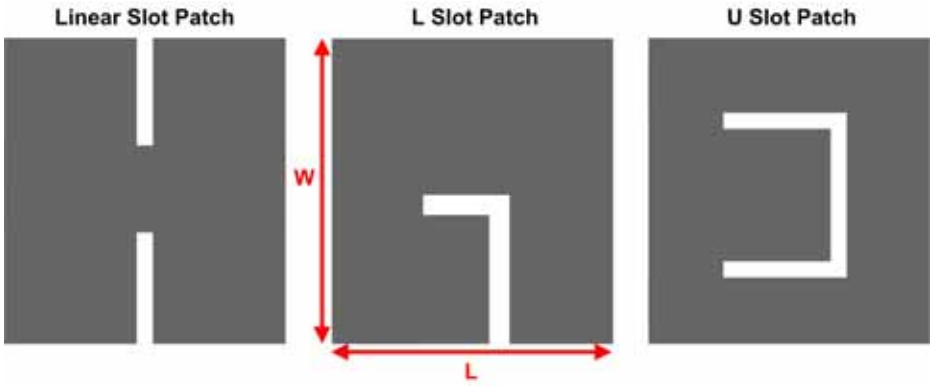

Fig. 15. Slot Geometries. Common slot geometries for microstrip patch loading

Whereas shorting and slot loading decrease the antenna's electrical size, dielectric loading reduces the physical size while maintaining the electrical size. High permittivity materials have been commonly employed in microstrip design to reduce size [53-54]. Recall the antenna size metric *ka*, which can be expressed more explicitly as:

$$ka = 2\pi f_r a\sqrt{\mu\varepsilon} \tag{10}$$

The propagation constant *k* can be increased and the antenna's physical size *a* decreased, with the product *ka*, the antenna's electrical size, remaining constant. Increasing permittivity ε effectively increases *k* while maintaining the resonant frequency f_r. Dielectric loading (ε) is preferred to ferrite loading (μ), due to the availability of

dielectric materials and high loss in magnetic materials. Assuming the resonant frequency remains constant, dielectric loading permits antenna miniaturization as in (11):

$$\frac{a'}{a} = \frac{1}{\sqrt{\varepsilon_r}} \tag{11}$$

where *a* is the antenna size without dielectric loading and *a'* is the antenna size with dielectric loading. Fig. 16 provides an illustration of the miniaturization achievable with high permittivity materials.

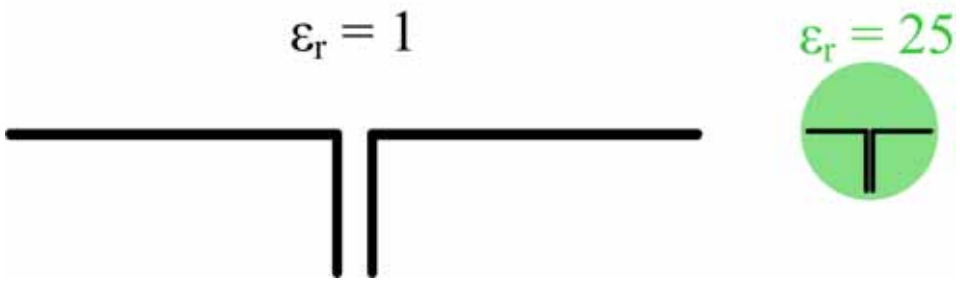

Fig. 16. Dielectric Loading. Antenna miniaturization via dielectric loading, to scale

D. Conformal Antennas

One of the earliest benefits of microstrip antenna technology was its compatibility with conformal geometries, which allowed microstrip integration into aerodynamic structures such as missiles and airplanes [55]. Several studies of cylindrically conformal microstrip patches indicate no performance change between flat and conformal operation, under the assumption that the substrate thickness $h << R$, with R the radius of curvature [56-57]. This result agrees with intuition, since the conformal

surface, whether cylindrical or spherical, appears planar as the radius of curvature increases. For the case of $h << R$, a modified cavity model, adapted to cylindrical or spherical boundary conditions, provides accurate results for the electric and magnetic fields [58]. The modified cavity model indicates a resonant frequency decrease of less than 5 % for $h < R/10$ [59].

Although a minor curvature has little effect on resonant frequency and input impedance, conformity has a greater impact on radiation. Curvature encourages the propagation of creeping waves, which strengthen back lobe radiation and broaden the radiation pattern [60-61]. The radiation pattern broadens and gain decreases as the radius of curvature R decreases [58, 61]. The effect of curvature on mutual coupling in conformal arrays and multiple element systems must be considered as well. Cavity-backed or recessed microstrip antennas effectively reduce coupling between elements [61-62]. For the more general case, with no limitations on substrate thickness h or radius of curvature R, the cavity model no longer applies, and changes in antenna parameters become more pronounced. Although theoretical models remain rare, due to the difficulty of modeling the patch in the presence of a small spherical or cylindrical scattering structure, experimental studies have revealed trends in antenna performance as the radius of curvature changes. For the case of curvature in one dimension (i.e. cylindrical conformity), the patch can be defined as either axially or circumferentially polarized [61, 63], depending on whether the curvature occurs across the patch width or length. Fig 17 provides a reference for these two cases. For circumferentially polarized patches

curvature occurs across the patch width (around Axis B), whereas curvature occurs across the patch length (around Axis A) for axially polarized patches.

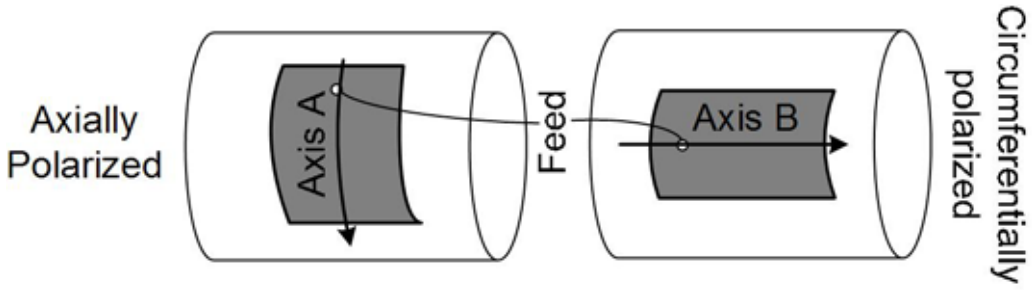

Fig. 17. Axial and Circumferential Polarization. Circumferential polarization occurs for curvature around Axis B, and axial polarization occurs for curvature around Axis A

For the circumferentially polarized case, the resonant frequency decreases as the radius of curvature decreases, but the antenna match remains stable. For the axially polarized case, the resonant frequency remains constant, but the antenna detunes [61, 63]. The results for cylindrical curvature apply to the spherical case as well, where both forms of curvature, axial and circumferential, occur simultaneously. For the *SIFA*, $h = R/4$, so the resonant frequency should decrease and detune slightly relative to a *PIFA* with equivalent design parameters.

CHAPTER III

THE SPHERICAL INVERTED-F ANTENNA

A. Physical Model

The *SIFA* will be analyzed from three different perspectives: a physical model, which allows insight into the field structure and highlights parallels with planar design, a modified transmission line model, which converts physical dimensions into equivalent circuit parameters, and a parameter sensitivity analysis, which maps the effect of varying design parameters on antenna performance and provides a qualitative guide for design**.** Fig. 18 illustrates the *SIFA*'s physical geometry, with significant design variables labeled.

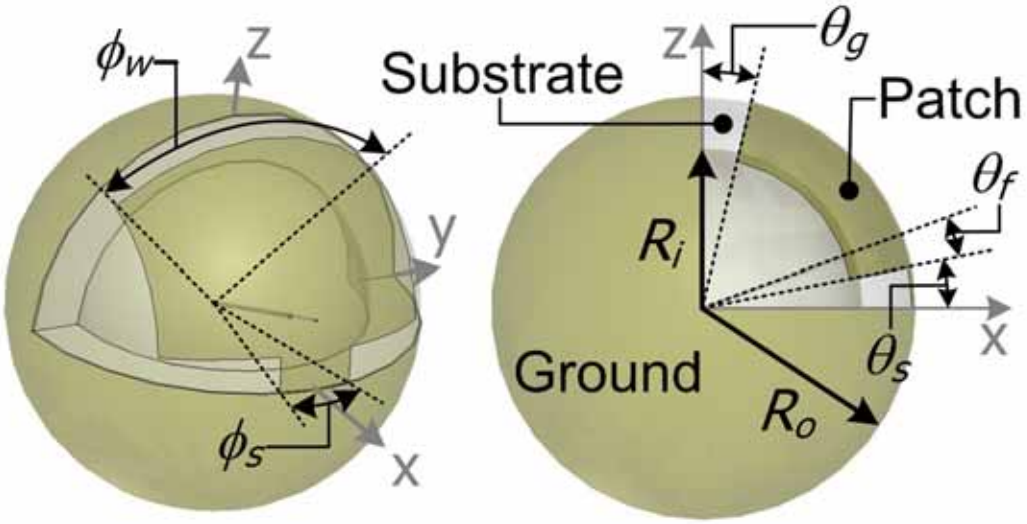

Fig. 18. *SIFA* Physical Model. Radii R_o and R_i determine antenna size and substrate thickness. Variables φ_w and φ_s determine patch width and short width, respectively. Elevation variables θ_g, θ_s, and θ_f determine the gap size, short size, and feed position, respectively

The outer radius R_o determines the antenna size and approximate operating frequency. Once the outer radius has been determined, the inner radius R_i controls the substrate thickness h according to $h = R_o - R_i$. Azimuthal variables φ_w and φ_s determine the patch width and short width, respectively, and elevation variables θ_g and θ_s tune the size of the top and bottom slots, respectively. The feed position θ_f alters the probe position in a similar manner to the planar case. Each angular variable corresponds to an equivalent arc length. The *SIFA* can be designed according to either convention. Eq. (12) provides conversions from angular variables to equivalent arc lengths, which will be used in the *SIFA* analytical model.

$$\begin{aligned} L_{g,s,f} &= 2\pi R_o \frac{\theta_{g,s,f}}{360^\circ} \\ W_{s,p} &= 2\pi R_o \frac{\phi_{s,p}}{360^\circ} \\ L_p &= \left(\frac{\pi}{2} R_o - L_s - L_g\right) \cos\left(\frac{\phi_p}{2}\right) \end{aligned} \tag{12}$$

The gap length L_g, short length L_s, and feed length L_f correspond to angular variables θ_g, θ_s, θ_f, respectively. The patch width W_p and short width W_s correspond to angular variables φ_p and φ_s, respectively. The patch length L_p, which corresponds to the length along the patch edge, is determined by the short length L_s and gap length L_g. For design in arc lengths, each dimension corresponds to a rectilinear dimension in a recessed *PIFA*. This correspondence allows the *PIFA* transmission line model to be adapted to the spherical case, based on a conversion from rectilinear coordinates to arc lengths.

B. Analytical Modeling Techniques

The *SIFA* analytical model adapts the *PIFA* model to the physical geometry described above. Fig 19 presents a modified transmission line model based on the equivalent arc lengths defined in the previous section. The effective patch length L_{peff} can be found from the patch length L_p, patch width W_p, and short width W_s according to $L_{peff} = L_p + \Delta L + (W_p - W_s)/2$, with ΔL given in (8). To simplify the derivation of slot admittance, the spherically conformal slots are replaced by slots with equivalent rectangular dimensions. This substitution uses the closed form expressions given in (6) to approximate the conformal slot admittance Y_{slot}. Appendix A provides a derivation of G_{ss} based on aperture theory and the Matlab code used to determine G_{ss} numerically. Appendix B provides the Matlab code used to evaluate the analytical model below.

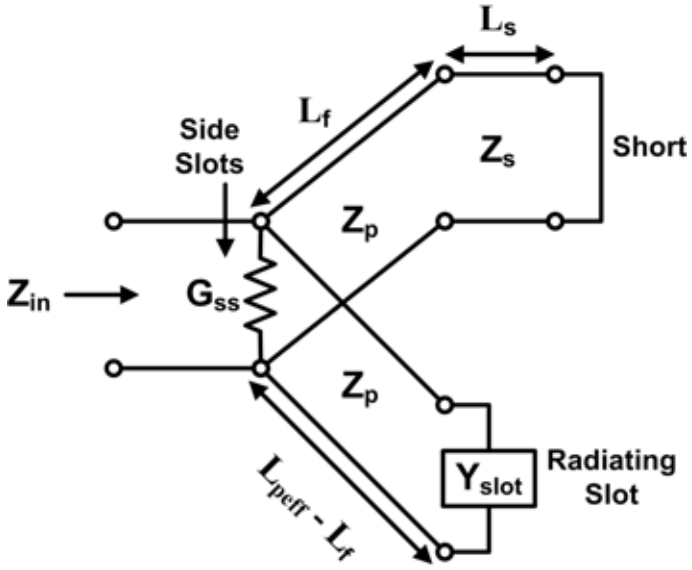

Fig. 19. *SIFA* Analytical Model. The short width W_s and patch width W_p determine the patch characteristic impedance Z_p and short characteristic impedance Z_s. Lengths L_f, L_s, and L_{peff} can be determined from the above conversions in a similar manner. The side slot conductance G_{ss} is determined from aperture theory, as outlined in Appendix A

Fig. 20 compares VSWR and Smith data from the analytical model to numerically simulated data for a *SIFA* with design parameters labeled in Table 1. The analytical model predicts a 384 MHz resonant frequency with a 34 MHz (8.9 %) bandwidth. Simulated data produces a 404 MHz resonant frequency with a 32 MHz (7.9 %) bandwidth, resulting in a 5 % frequency difference between the analytical model and simulation. Several effects explain the difference between analytical and simulated results. The analytical model calculates slot admittance based on rectilinear dimensions, thus neglecting slot curvature over the spherical surface. Furthermore, the recessed structure increases capacitance at the radiating edges, but the model assumes the same capacitance as a non-recessed structure. The transmission line parameters Z_p and Z_s depend on planar microstrip design equations, without adjustment for spherical conformity. Results indicate that the analytical model provides an accurate first-order approximation for *SIFA* operation that requires fine tuning via numerical simulation.

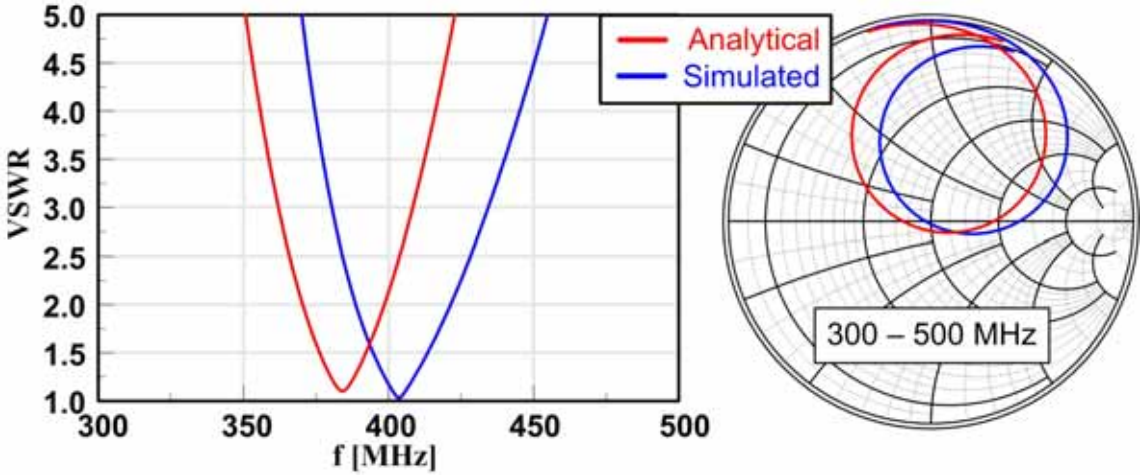

Fig. 20. Analytical Model Results. A comparison of analytical and simulated results for the fabricated *SIFA*. The results differ as a result of simplifications in the analytical model

Table. 1. Analytical Model *SIFA* parameters

Parameter	Variable	Value
Outer Radius	R_o	**101.6 mm**
Inner Radius	R_i	**76.2 mm**
Feed Angle	θ_f	**9°**
Slot Length Angle	θ_g	**13°**
Short Length Angle	θ_s	**11°**
Short Width Angle	φ_s	**22°**
Patch Width Angle	φ_w	**45°**

B. Parameter Sensitivity Study

Although analytical modeling allows a first-order approximation of SIFA operation, numerical simulation provides an effective tool for fine tuning the design. A parameter sensitivity study aids in the tuning process by compiling the impedance response to changes in various design parameters. Fig. 21 provides parameter sensitivity data for five primary design variables. As the inner radius R_i increases, the substrate height decreases, and the patch characteristic impedance Z_p decreases, causing the impedance locus to move into the low resistance region of the Smith Chart. Increasing the short width φ_s increases the inductance and causes the impedance locus to contract into the top half of the Smith chart. As the feed location θ_f decreases, the feed moves closer to the short, increasing the inductance seen by the probe; as a result, decreasing the feed angle θ_f and increasing the short width φ_s produce similar effects. As the gap sizes θ_g and θ_s increase, the top radiating slot becomes less capacitive, but the short moves farther from the feed as well, reducing the inductance. The results in Fig. 21 indicate that the decrease in inductance overwhelms the reduced capacitance, causing the impedance locus to expand into the capacitive region of the Smith chart. The gap lengths

are not necessarily equal, but were often assigned the same value to simplify the design process. Furthermore, θ_g and θ_s provide fine tuning for the resonant frequency, since the gap lengths determine the patch length L_p. The trends revealed by the parameter sensitivity study support the analytical model developed previously.

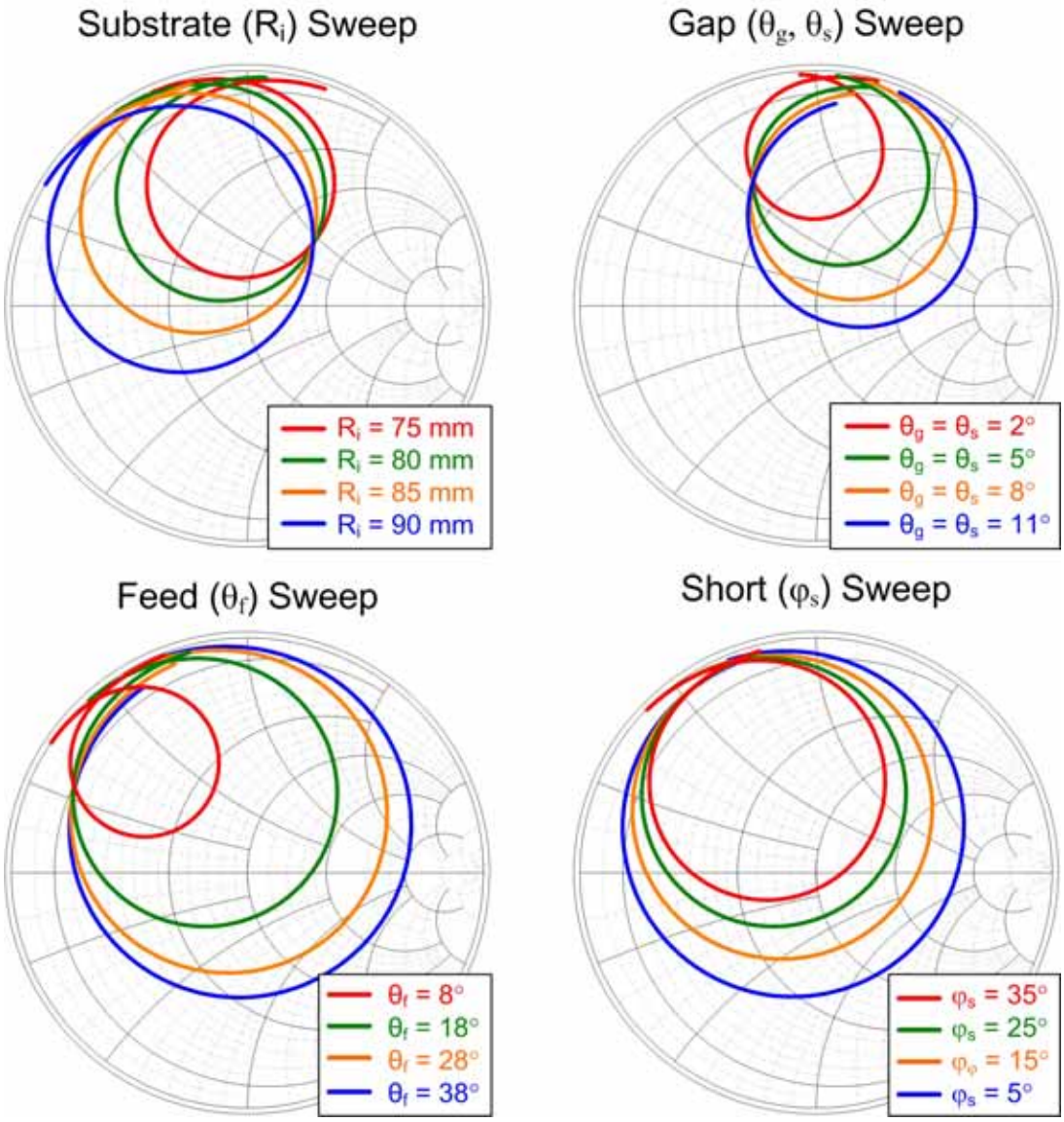

Fig. 21. Parameter Sensitivity Study. Increasing R_i moves the impedance locus into the lower resistance region of the Smith Chart. Increasing θ_g and θ_s simultaneously broadens the impedance locus into the capacitive region of the Smith chart. Increasing θ_f or φ_s causes the impedance locus to broaden into the capacitive region of the Smith chart

CHAPTER IV

FABRICATED ANTENNA

A. Fabrication Process

To verify the analytical and numerical design processes, the *SIFA* was fabricated with Styrofoam spheres and solder-tacked copper tape. The dimensions of available Styrofoam spheres limited the choice of outer radius R_o to 101.6 mm (4”) and inner radius R_i to 76.2 mm (3”). The fabricated design used angular design parameters (as shown in Table 1) based on the analytical and numerical simulation, which assumed a relative Styrofoam permittivity of 1.03. Fig. 22 provides a diagram of the fabrication process. The fabrication procedure follows:

- A quarter section is removed from both the larger (4”) and smaller (3”) spheres.
- The quarter section of the larger sphere is hollowed out to create the antenna substrate and accommodate the quarter section of the smaller sphere, which becomes part of the ground plane (Fig. 22 - A).
- The quarter section of the smaller sphere is inserted into the remaining section of the larger sphere. The entire structure is coated with copper tape to create the ground plane and host structure. The copper tape is tacked with solder to ensure continuity of current flow (Fig. 22 - B).
- A semi-rigid coaxial cable is fed through the back side of the sphere and the outer conductor is soldered to the ground structure, both at the back of the ground

plane and where the probe excitation emerges beneath the patch structure (Fig. 22 - C).

- The patch geometry (including the shorting strip) is formed on the Styrofoam substrate and placed into the host structure. The patch is solder-tacked with for electrical continuity and the center conductor of the semi-rigid coaxial cable is soldered to the patch surface (Fig. 22 - D).

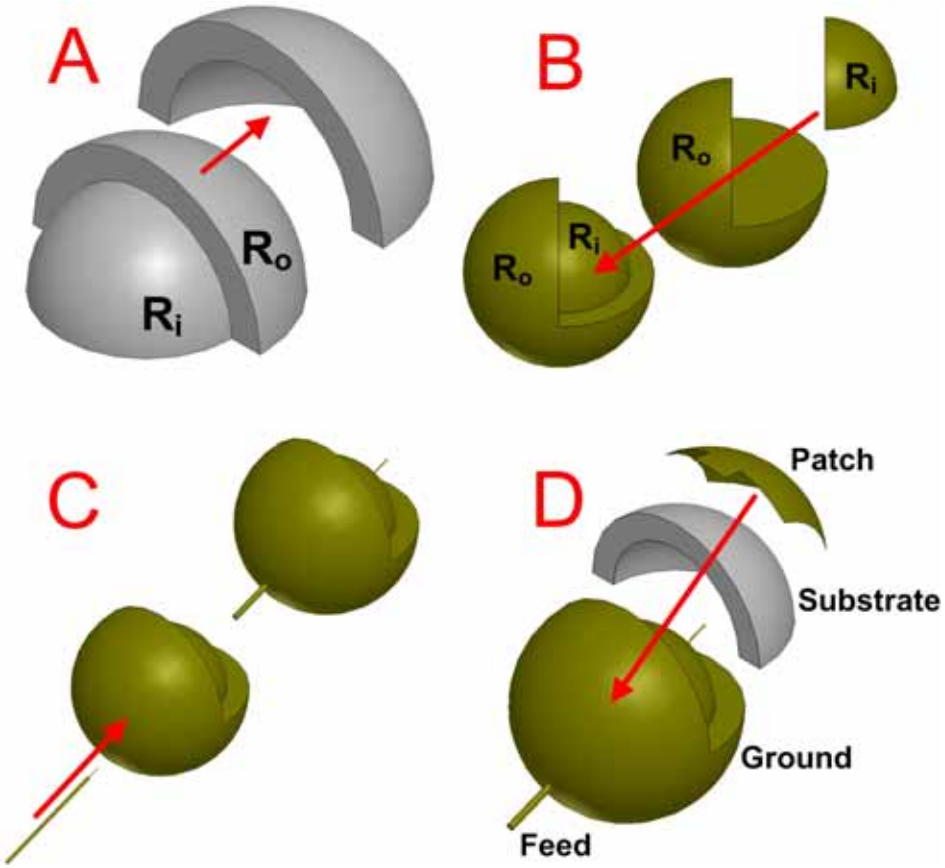

Fig. 22. *SIFA* Fabrication Process. A - Forming antenna substrate. B - Insertion of inner sphere into outer sphere to create ground structure/host chassis. C - Coaxial probe excitation with semi-rigid coax. D - Final assembly of all components

The fabricated *SIFA* dimensions were measured and compared with simulated dimensions to explain any differences between simulated and measured results. The simulated and measured dimensions of the fabricated *SIFA* have been provided in Table 2, which indicates that fabricated and simulated dimensions match well; nonetheless, some potential for error exists in the measurement of fabricated dimensions due to the difficulty of measuring spherical arc lengths. The fabricated *SIFA* can be seen in Fig. 23.

Table. 2. Simulated and Fabricated *SIFA* parameters

Parameter	Variable	Simulated Value	Fabricated Value
Outer Radius	R_o	**101.6 mm**	**101.6 mm**
Inner Radius	R_i	**76.2 mm**	**76.2 mm**
Feed Angle	θ_f	**9°**	**7°**
Slot Length Angle	θ_g	**13°**	**13°**
Short Length Angle	θ_s	**11°**	**11°**
Short Width Angle	φ_s	**22°**	**22°**
Patch Width Angle	φ_w	**45°**	**45°**

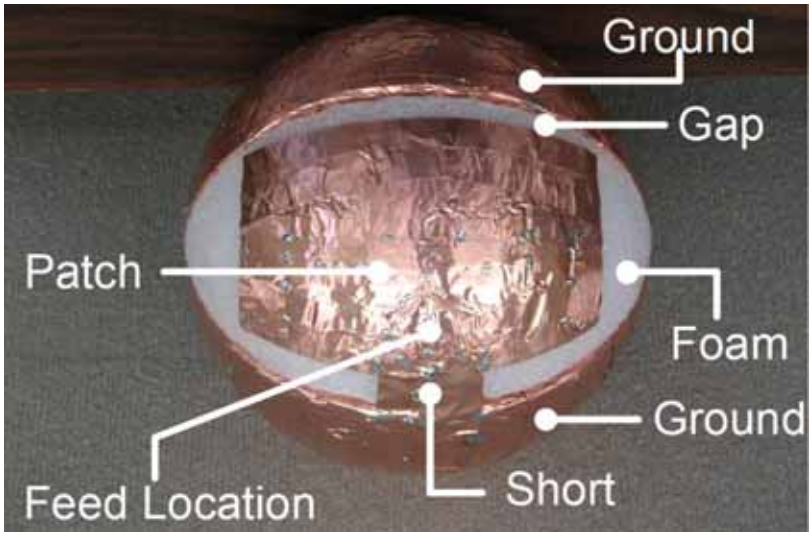

Fig. 23. Fabricated *SIFA*. The ground and patch structures were formed with copper tape

B. Results

Fig. 24 shows impedance and VSWR measurements of the fabricated *SIFA* with simulated results superimposed for comparison. The fabricated antenna operates at 407 MHz with a 19 MHz (4.7 %) bandwidth and fully incorporates the MICS band (402 - 405 MHz). The measured results match well with simulated data, which gives a resonant frequency of 404 MHz with a 32 MHz (7.9 %) bandwidth. Comparison of measured and simulated data on the Smith chart verifies the VSWR result. The impedance locus of the measured data has contracted slightly relative to the simulated data.

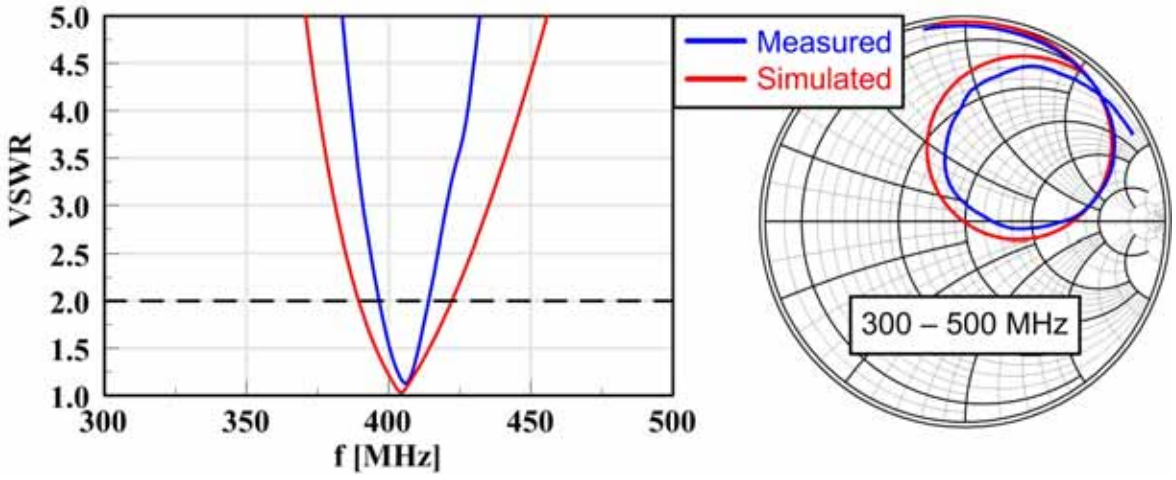

Fig. 24. *SIFA* - Measured and Simulated VSWR and Smith Response. Simulation results in a resonant frequency of 404 MHz with a 32 MHz (7.9 %) bandwidth, and measurements produce a resonant frequency of 407 MHz with a 19 MHz (4.7 %) bandwidth

The resonant frequency difference between simulation and fabrication is less than 1 %, but the bandwidth of the fabricated design decreases significantly relative to simulated results. The potential for a small fabrication error in each dimension, compounded with the number of design variables, accounts for the slight difference in

performance. Although the dimensions agree well in Table 2, the difficulty of measuring angular design variables allows significant potential for error. The inner radius R_i, although measured as 76.2 mm before fabrication, could have been altered during the fabrication process. R_i could not be measured after fabrication without dismantling the *SIFA*. Based on the comparison of simulated and fabricated dimensions in Table 2, a slight error in coaxial feed placement was the probable cause of differences between simulated and measured data. Fig. 25 provides simulated radiation patterns, in the three primary cut planes, for the design under consideration. Due to frequency limitations of available anechoic facilities, measured radiation patterns are not available.

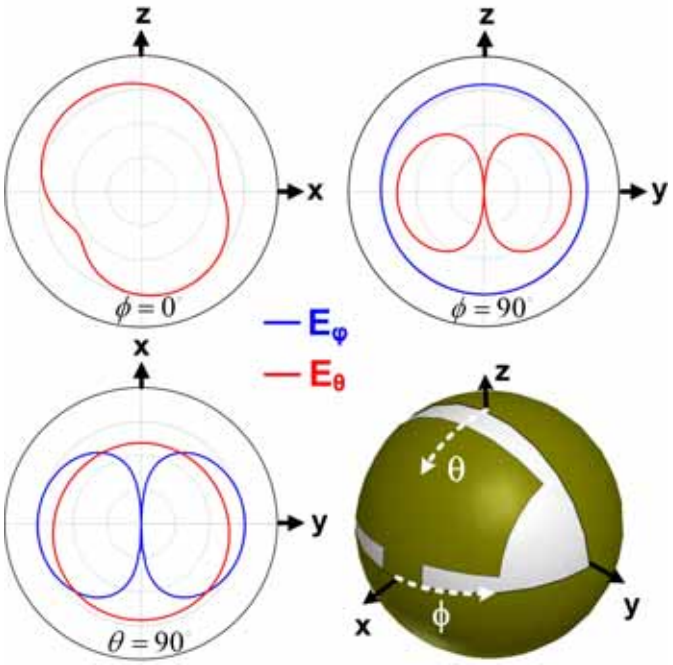

Fig. 25. *SIFA* - Simulated Radiation Patterns. Simulated radiation patterns for the fabricated *SIFA* design, plotted over a minimum -30 dB, maximum 10 dB, with 10 dB divisions. As expected, the patterns evidence significant back lobe radiation and enhanced omni-directionality compared to planar microstrip antennas

The radiation patterns indicate that the *SIFA* operates in a similar manner to a *PIFA*, with spherical conformity resulting in significant backlobe radiation and enhanced omni-directionality. Fig. 26, which shows the resonant field structure in the substrate, confirms this result. The φ = 0° elevation pattern shows the θ-polarized radiation from the primary radiating slot, which is located opposite the short. The φ = 90° elevation pattern shows the φ-polarized radiation from the primary radiating slot, with the side slots contributing the cross polarization (θ-polarized). The null in cross polarization occurs along a plane equidistant from the two side slots. The azimuthal plane follows the same trend.

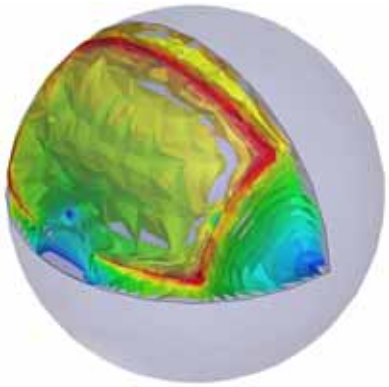

Fig. 26. *SIFA* - Field Structure. Resonant field structure in the fabricated *SIFA*. The top slot provides primary radiation, but the side slots contribute as well

CHAPTER V

ONGOING AND FUTURE WORK

Although the original *SIFA* design performs well in the MICS band, the antenna remains physically large (R_o = 101.6 mm) and relatively limited in application. Several modifications improve performance and expand the application space. Slot loading and dielectric coating achieve antenna miniaturization (both electrical and physical), and the introduction of multiple elements on the host structure allows dual band operation and beam steering. Incorporating both slot loading and dielectric coating miniaturizes the *SIFA* to a reasonable pill size for capsule endoscopy and other ingestible applications. The miniaturized *SIFA*, which operates at MICS band, performs well in the majority of biological media.

A. Slot Loading

Slot loading has enabled *PIFA* miniaturization down to $\lambda/8$ or even $\lambda/16$ [48-50]. Following fabrication of the original *SIFA*, slots were introduced into the patch geometry to reduce antenna size. A first design introduced linear slots in the patch center, as shown in Fig. 27. Two new design variables θ_{ss} and φ_{ss} define the slot width and length, respectively. Existing parameters are retuned to account for the affect of slot loading. Table 3 provides values for the design parameters labeled in Fig. 27, as well as the original *SIFA* parameters. Fig. 28 presents VSWR and Smith data for the linear slotted design, and simulated radiation patterns can be seen in Fig. 29. The side slots achieve a

20 % reduction in resonant frequency (f_r = 324.5 MHz) as the *SIFA* radius remains constant. The bandwidth decreases to 2.77 % (9 MHz) as the electrical size decreases to ka = 0.69. The radiation patterns strongly resemble those of the original *SIFA*. The patterns show no increase in cross polarization, since the two slots produce equivalent magnetic currents with opposite phase in close proximity. Furthermore, the slots run parallel to the primary radiating slot, reducing their contribution to cross polarized fields.

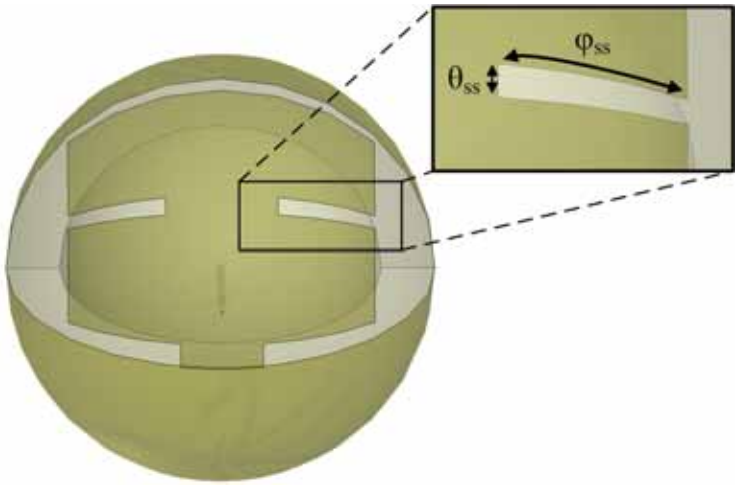

Fig. 27. Linear Slotted *SIFA* - Physical Geometry. New design parameters are slot width θ_{ss} and slot length φ_{ss}

Table. 3. Linear Slotted *SIFA* - Design Parameters

Parameter	Variable	Value
Outer Radius	R_o	101.6 mm
Inner Radius	R_i	76.2 mm
Feed Angle	θ_f	9°
Slot Length Angle	θ_g	5°
Short Length Angle	θ_s	5°
Short Width Angle	φ_s	22°
Patch Width Angle	φ_w	45°
Slot Width Angle	θ_{ss}	5°
Slot Length Angle	φ_{ss}	40°

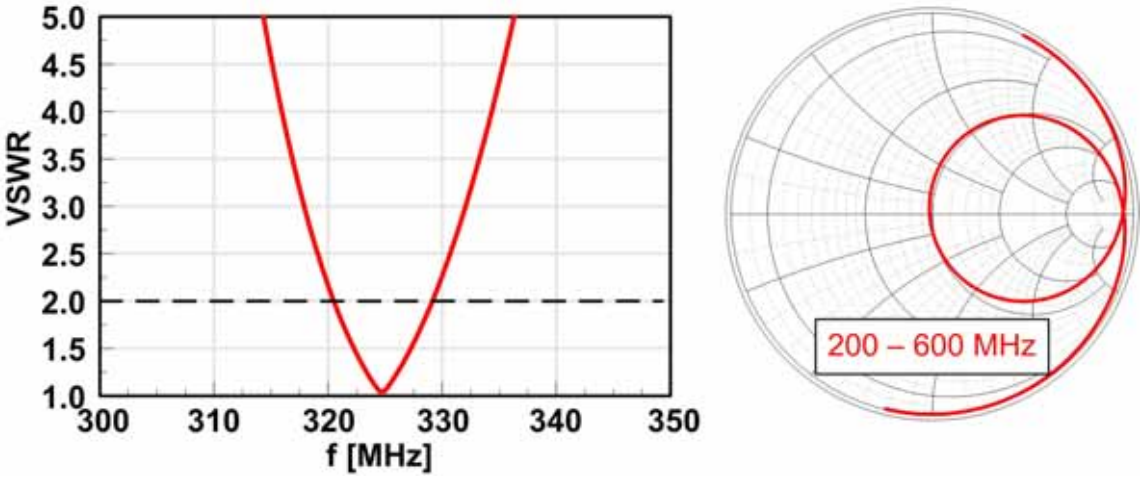

Fig. 28. Linear Slotted *SIFA* - VSWR and Smith Response. The *SIFA* achieves a 20 % reduction in resonant frequency relative to the original design

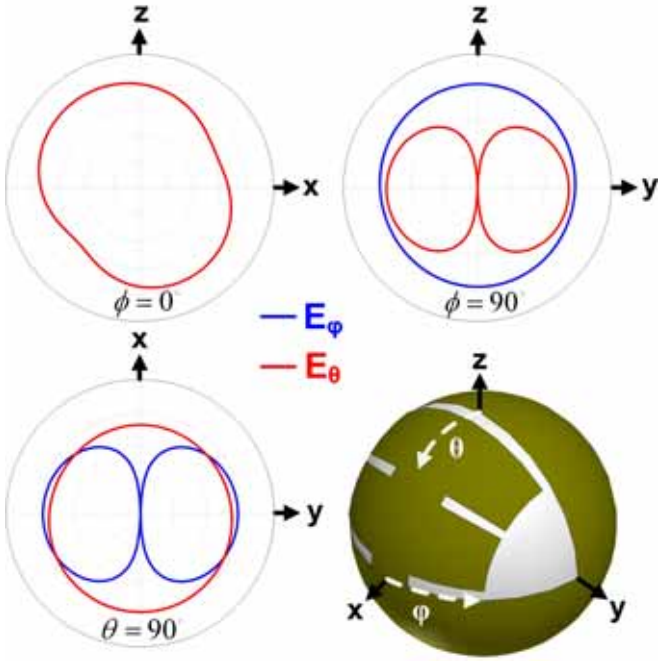

Fig. 29. Linear Slotted *SIFA* - Radiated Fields. Radiation patterns in the three primary cut planes for the slotted *SIFA*, plotted over a minimum -30 dB, maximum 10 dB, with 10 dB divisions

L slots were compared with the linear slots presented above to determine which geometry achieved the greatest reduction in resonant frequency. An initial design

introduced a single L-shaped slot along on side of the patch, as shown in Fig. 30. The existing design variables remain, with θ_L introduced to represent the length of the new slot segment. Both sections of the L slot have the same width θ_{ss}. Table 4 provides the parameters for this design. Fig. 31 shows the VSWR and Smith data for the single L slotted *SIFA*, and simulated radiation patterns can be seen in Fig. 32. The L slot reduces resonant frequency by 20 % (f_r = 326 MHz) as the *SIFA* radius remains constant. The bandwidth decreases to 2.45 % (8 MHz) as the electrical size decreases to ka = 0.69. The single L slot and dual linear slots achieve an almost identical reduction in resonant frequency and bandwidth. The radiation patterns for the L slotted *SIFA* show increased cross polarization (φ-polarized) in the φ = 0° plane relative to the linear slotted and original *SIFA* designs, as well as a slight tilt in the cross polarization (θ-polarized) in the φ = 90° plane. The increased cross-polarization can be attributed to the addition of the L slot perpendicular to the primary radiating slot.

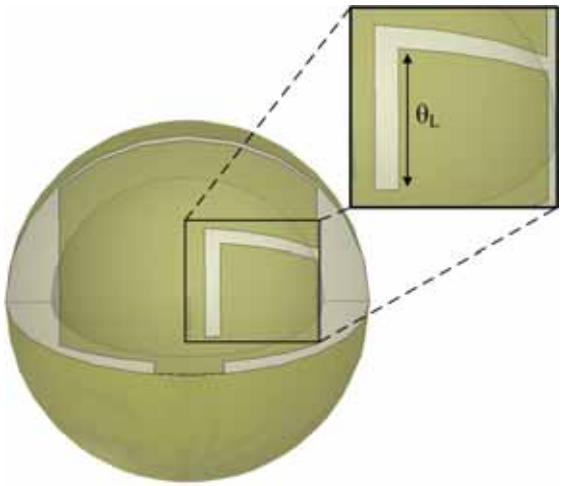

Fig. 30. Single L Slot *SIFA* - Physical Geometry

Table. 4. Single L Slotted *SIFA* – Design Parameters

Parameter	Variable	Value
Outer Radius	R_o	101.6 mm
Inner Radius	R_i	76.2 mm
Feed Angle	θ_f	9°
Slot Length Angle	θ_g	4°
Short Length Angle	θ_s	4°
Short Width Angle	φ_s	22°
Patch Width Angle	φ_w	45°
Slot Width Angle	θ_{ss}	5°
Slot Length Angle	φ_{ss}	40°
L-Slot Length Angle	θ_L	30°

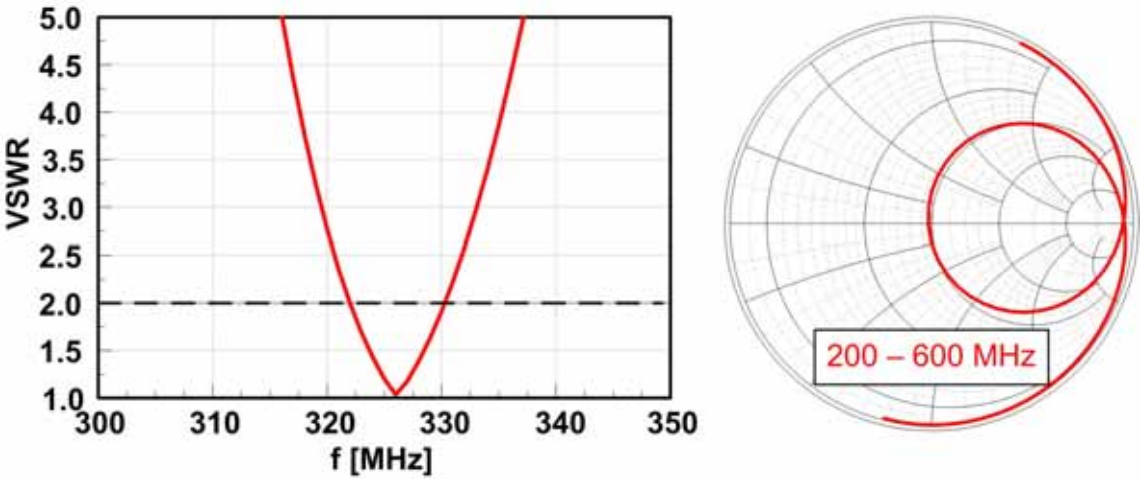

Fig. 31. Single L Slot *SIFA* - VSWR and Smith Response. The resonant frequency and bandwidth mirror those of the previous design, which utilized two linear slots

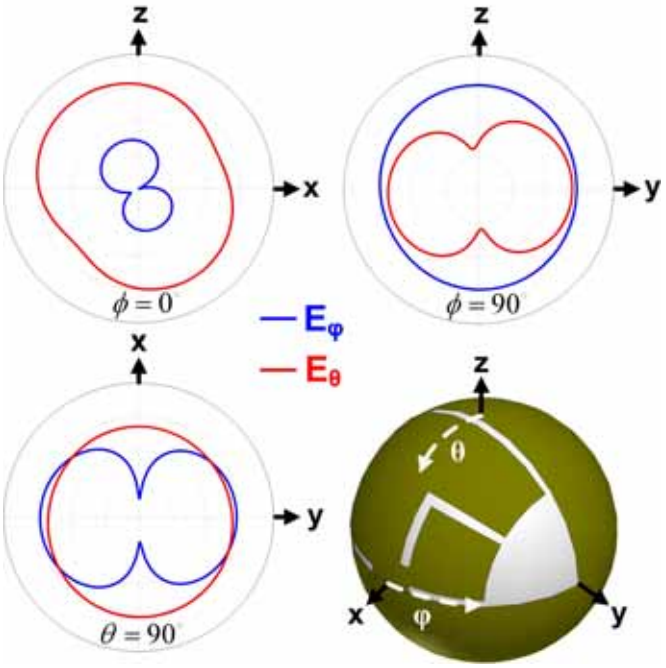

Fig. 32. Single L Slot *SIFA* - Radiated Fields. Radiation patterns in the three primary cut planes for the single L slotted *SIFA*, plotted over a minimum -30 dB, maximum 10 dB, with 10 dB divisions. Cross polarization increases in the φ = 0° plane due to the L slot perpendicular to the primary radiating slot

To further reduce the resonant frequency, an identical L slot was introduced into the other side of the patch. The slot parameters were held constant and the feed angle θ_f, short width φ_s, and gap lengths θ_g and θ_s tuned to match. Table 5 displays the resulting design parameters. Introducing slots into the antenna effectively increases the inductance, since the slots create areas of high current density as the current follows the slot contour. To compensate for the inductive effect of the slots, the capacitance of at the patch edges is increased by decreasing gap sizes θ_g and θ_s. Thus, as the slotted design has progressed from linear slots to single and dual L slots, the gap lengths θ_g and θ_s have decreased to offset the increasing inductance. Since the *SIFA* remains confined to a

quarter section of the spherical surface, decreasing the gap lengths serves as a limited compensation mechanism.

Table. 5. Dual L Slotted *SIFA* - Design Parameters

Parameter	Variable	Value
Outer Radius	R_o	**101.6 mm**
Inner Radius	R_i	**76.2 mm**
Feed Angle	θ_f	**7.5°**
Slot Length Angle	θ_g	**2°**
Short Length Angle	θ_s	**2°**
Short Width Angle	φ_s	**70°**
Patch Width Angle	φ_w	**45°**
Slot Width Angle	θ_{ss}	**5°**
Slot Length Angle	φ_{ss}	**40°**
L-Slot Length Angle	θ_L	**30°**

Fig. 33 provides the VSWR and Smith data for the dual L slotted *SIFA*. The L slot reduces resonant frequency by 37 % (f_r = 254.5 MHz) as the *SIFA* radius remains constant. The bandwidth decreases to 0.78 % (2 MHz) as the electrical size decreases to ka = 0.54. Dual L slots achieve approximately twice as much reduction in resonant frequency as the single L slot and dual linear slots.

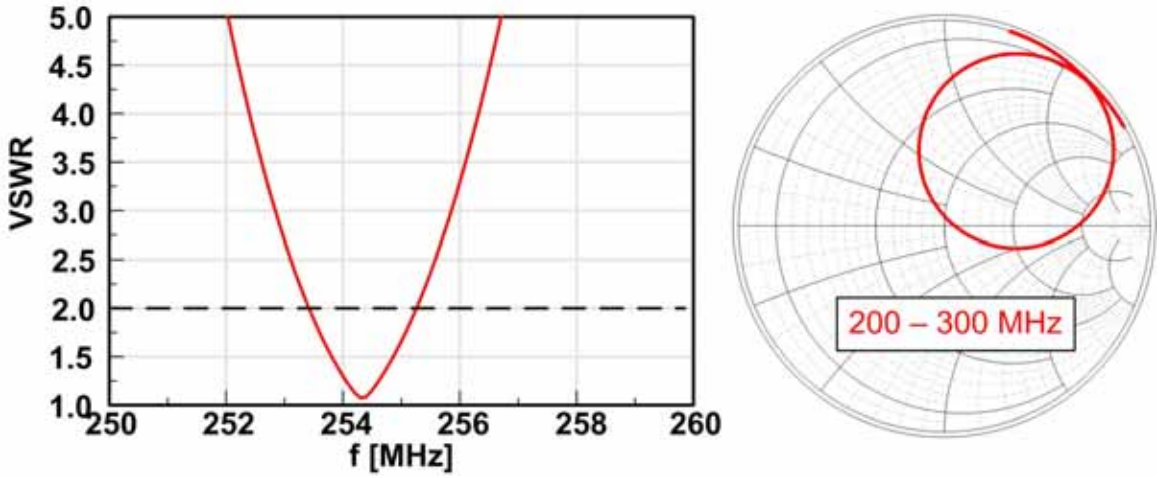

Fig. 33. Dual L Slot *SIFA* - VSWR and Smith Response. The *SIFA* achieves a 37 % decrease in resonant frequency relative to the original *SIFA* design

Fig. 34 provides the radiation patterns for the dual L slotted *SIFA*, which shows a similar level of cross polarization (φ-polarized) in the φ = 0° plane as the original *SIFA* design. The decrease in cross polarization between the single L and dual L slot designs can be attributed to slot symmetry. For the dual L slot design, each slot's radiation cancels that of the other slot, whereas the single L slot radiates without cancellation. The dual L slotted *SIFA* increases the θ-polarization in the φ = 90° plane in a similar manner to the single L slotted *SIFA*. Integrating slots into the patch geometry significantly reduces resonant frequency while maintaining the original *SIFA* size. Alternatively, slot integration allows *SIFA* miniaturization while maintaining the original resonant frequency. All three slotted designs fell in the electrically small region ($ka < 1$).

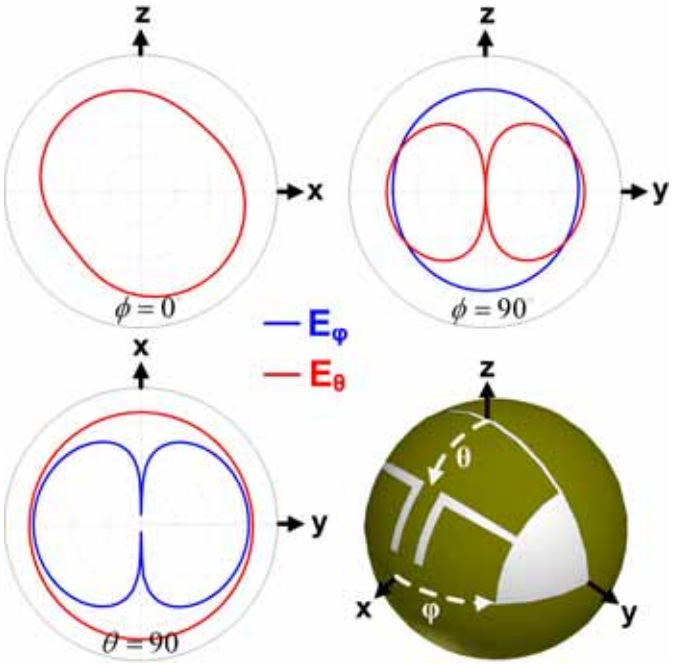

Fig. 34. Dual L Slot *SIFA* - Radiated Fields. Radiation patterns in the three primary cut planes for the dual L slotted *SIFA*, plotted over a minimum -30 dB, maximum 10 dB, with 10 dB divisions

B. Multiple Antenna Techniques

The *SIFA*'s spherical geometry encourages the use of multiple elements, which can provide operation in multiple bands, phased array behavior, or both. A few designs were investigated to highlight potential applications of multiple elements. The first design examines the effectiveness of two identical elements in enhancing radiation behavior. The design uses the original *SIFA* geometry, with two elements placed on opposite sides of the host chassis (180° apart), as can be seen in Fig. 35. Both elements use the same design values as the original *SIFA*, except for feed position, which was tuned to account for mutual coupling effects. Table 6 lists the design parameters.

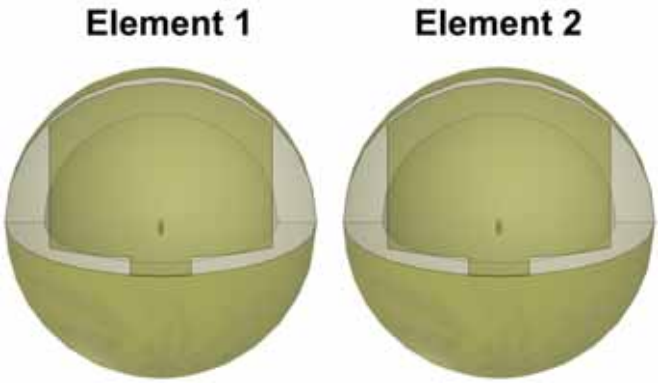

Fig. 35. Two Element *SIFA* - Physical Geometry. The two elements are identical and located on opposite sides of the sphere

Table. 6. Multiple Elements - Pattern Control

Parameter	Variable	Value
Outer Radius	R_o	101.6 mm
Inner Radius	R_i	76.2 mm
Feed Angle	θ_f	5°
Slot Length Angle	θ_g	13°
Short Length Angle	θ_s	11°
Short Width Angle	φ_s	22°
Patch Width Angle	φ_w	45°

Fig 36 presents the VSWR and Smith chart response for both elements, as well as the mutual coupling between the two elements. The VSWR and Smith response is the same for both elements, since both antennas see the same environment. Both elements operate at MICS band (f_r = 407 MHz) with a 5.1 % (21 MHz) bandwidth. Substantial coupling occurs, with a peak of -5 dB at the operating frequency. Coupling reduces the design's effectiveness, since a significant portion of the power leaving each element returns to the device through the other port, rather than radiating into free space.

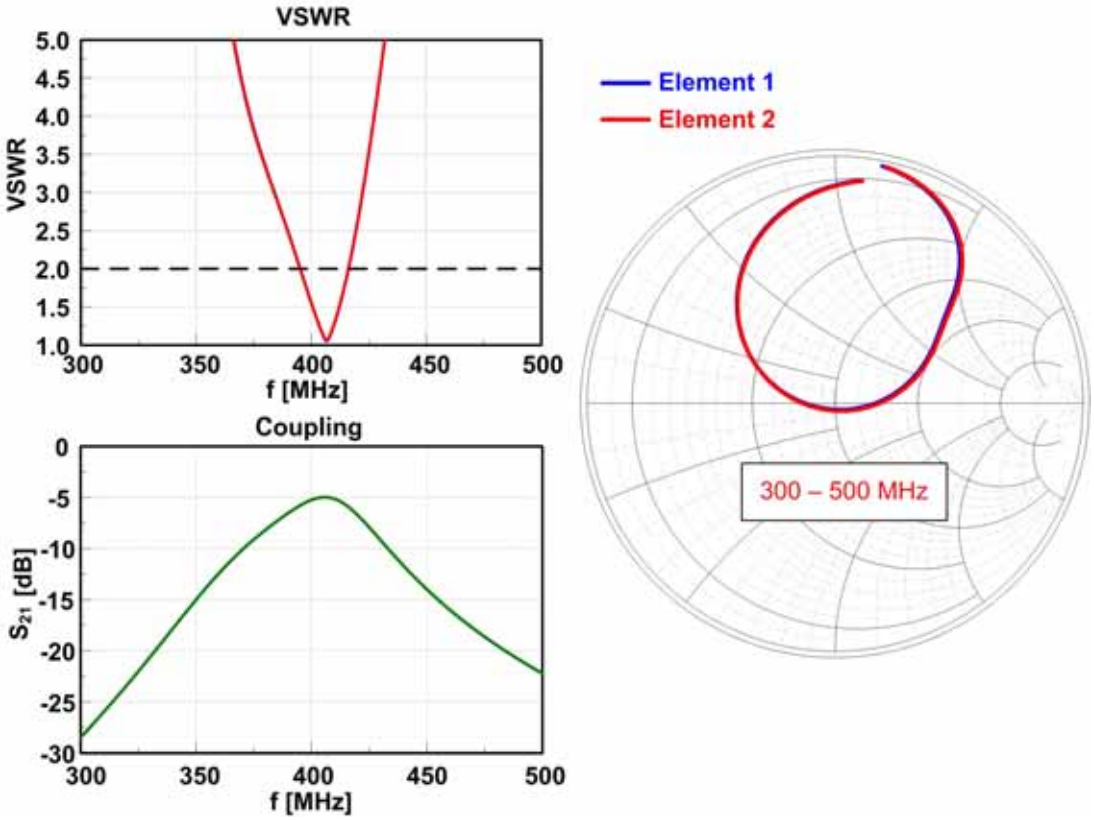

Fig. 36. Two Element *SIFA* - VSWR, Coupling, and Smith Response. The design maintains match at MICS band, but the mutual coupling degrades performance at the resonant frequency

Although mutual coupling degrades the design effectiveness, improved radiation patterns allow phased array behavior. Fig. 37 provides the radiation patterns in two configurations - with both elements in phase, and with the elements phased 180° relative to one another. The φ = 0° plane shows a significant amount of beam steering as the array switches from broadside to end-fire operation.

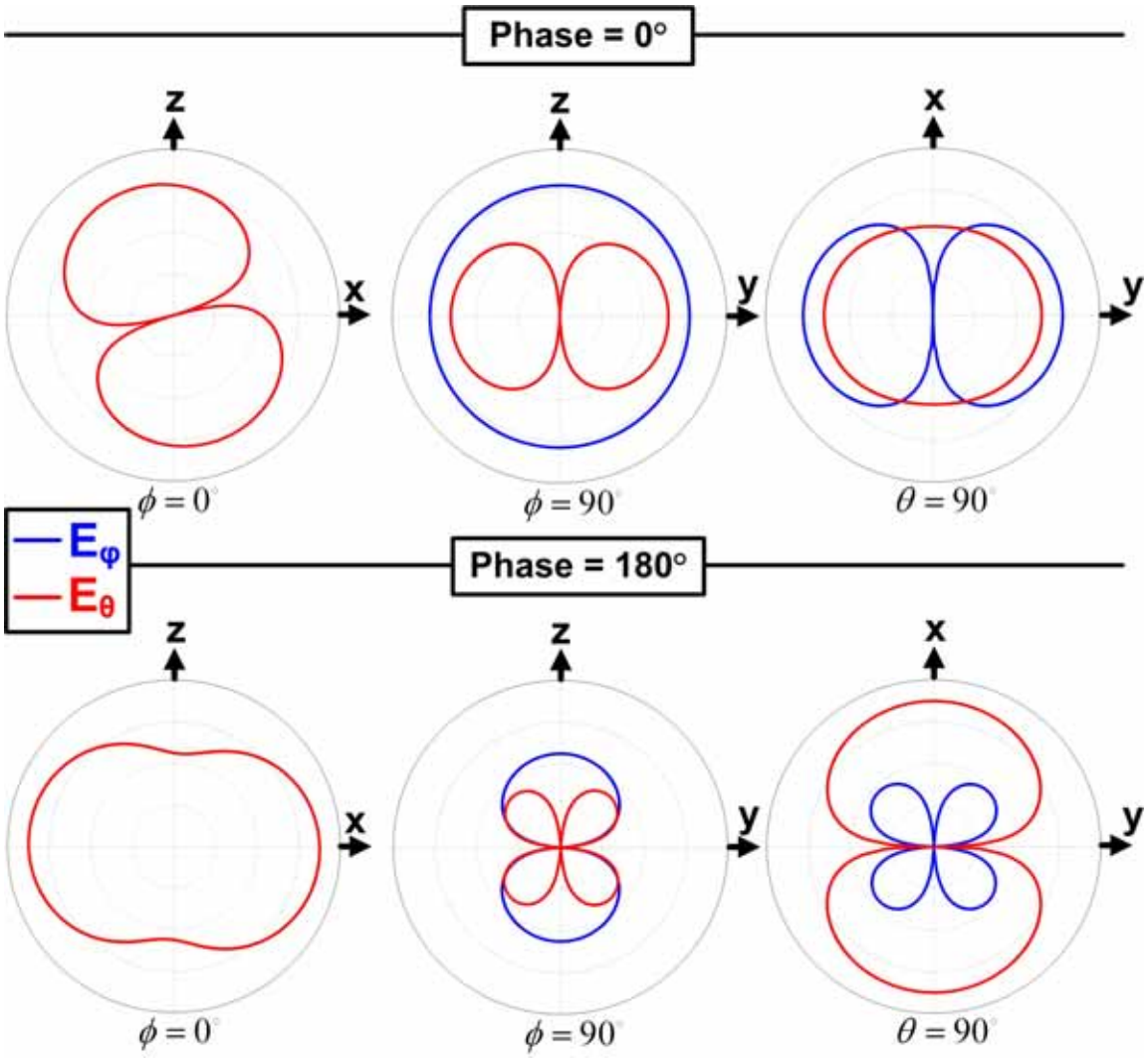

Fig. 37. Two Element *SIFA* - Radiated Fields. Radiation patterns for the two element *SIFA* with elements in phase and 180° out of phase, plotted over a minimum -30 dB, maximum 10 dB, with 10 dB divisions. The pattern reconfiguration between the two states indicates the potential for beam steering with multiple elements

To overcome mutual coupling, another design considers two elements with different geometries and resonant frequencies. The design uses the original *SIFA* patch geometry for one element and the linear slotted design, presented in Fig. 27, for the other element. The two elements are placed on opposite sides of the host chassis (180° apart), as can be seen in Fig. 38. The two elements use the same design values as their original

counterparts, except for feed position, which was tuned to account for mutual coupling effects. Table 7 provides the design parameters.

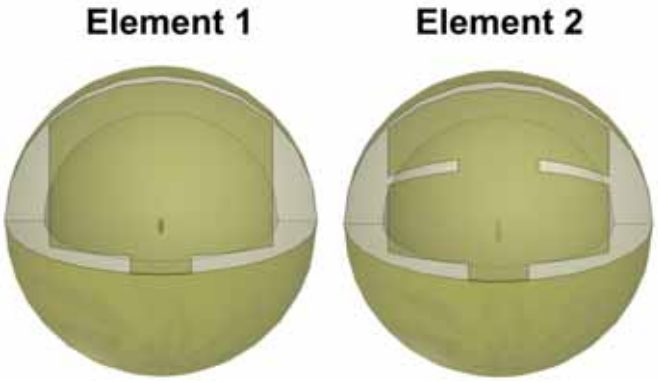

Fig. 38. Two Element Slotted *SIFA* - Physical Geometry. Element 1 is a variation of the original *SIFA* design, and element 2 is a variation of the linear slotted *SIFA*. The elements are located on opposite sides of the sphere

Table. 7. Multiple Elements - Dual Band Operation. Element 1 is identical to the original *SIFA*, except for feed tuning. Element 2 is identical to the linear slotted *SIFA*, except for feed tuning

Parameter	Variable	Element 1 Value	Element 2 Value
Outer Radius	R_o	101.6 mm	101.6 mm
Inner Radius	R_i	76.2 mm	76.2 mm
Feed Angle	θ_f	4°	1°
Slot Length Angle	θ_g	13°	5°
Short Length Angle	θ_s	11°	5°
Short Width Angle	φ_s	22°	22°
Patch Width Angle	φ_w	45°	45°
Slot Width Angle	θ_{ss}	N/A	5°
Slot Length Angle	φ_{ss}	N/A	40°

Fig. 39 presents the VSWR and Smith chart response for both elements, as well as the mutual coupling. The *SIFA* operates in two distinct bands, with the slotted *SIFA* operating in the lower band (f_r = 305 MHz) with a 2.6 % (8 MHz) bandwidth, and the

original *SIFA* operating in the upper band (f_r = 392.5 MHz) with a 5.6 % (22 MHz) bandwidth. Coupling decreases drastically relative to the previous design, with a peak of -15 dB at the lower band. The operating frequency of each element decreases slightly, by approximately 6 % for the slotted antenna and 3 % for the original *SIFA*, relative to the resonant frequency of each antenna alone.

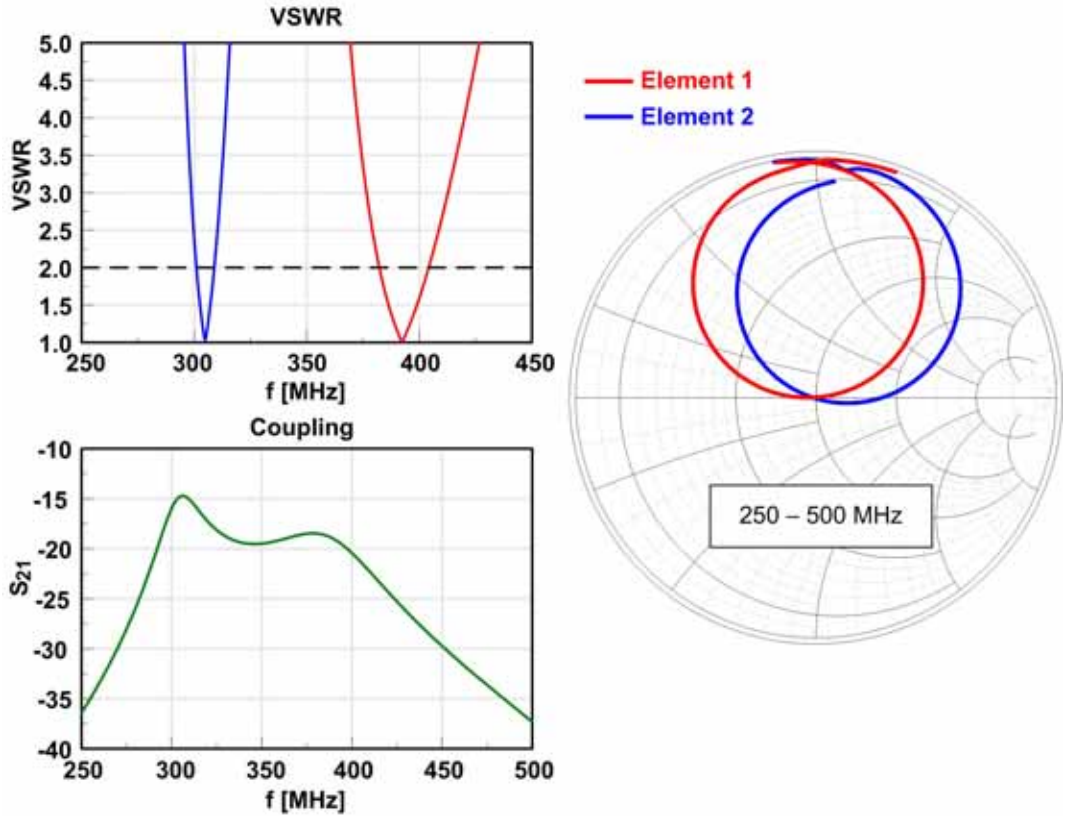

Fig. 39. Two Element Slotted *SIFA* - VSWR, Coupling, and Smith Response. The coupling decreases relative to the original two element *SIFA* due to the difference in frequency bands. Each element's resonant frequency shifts slightly relative to the original element in isolation

Fig. 40 provides the radiation patterns at each frequency (305 MHz and 392.5 MHz). The patterns change relative to those of each antenna in an isolated environment

because of modifications in the host chassis structure and coupling between the elements; nonetheless, the general radiation characteristics remain the same for both antennas.

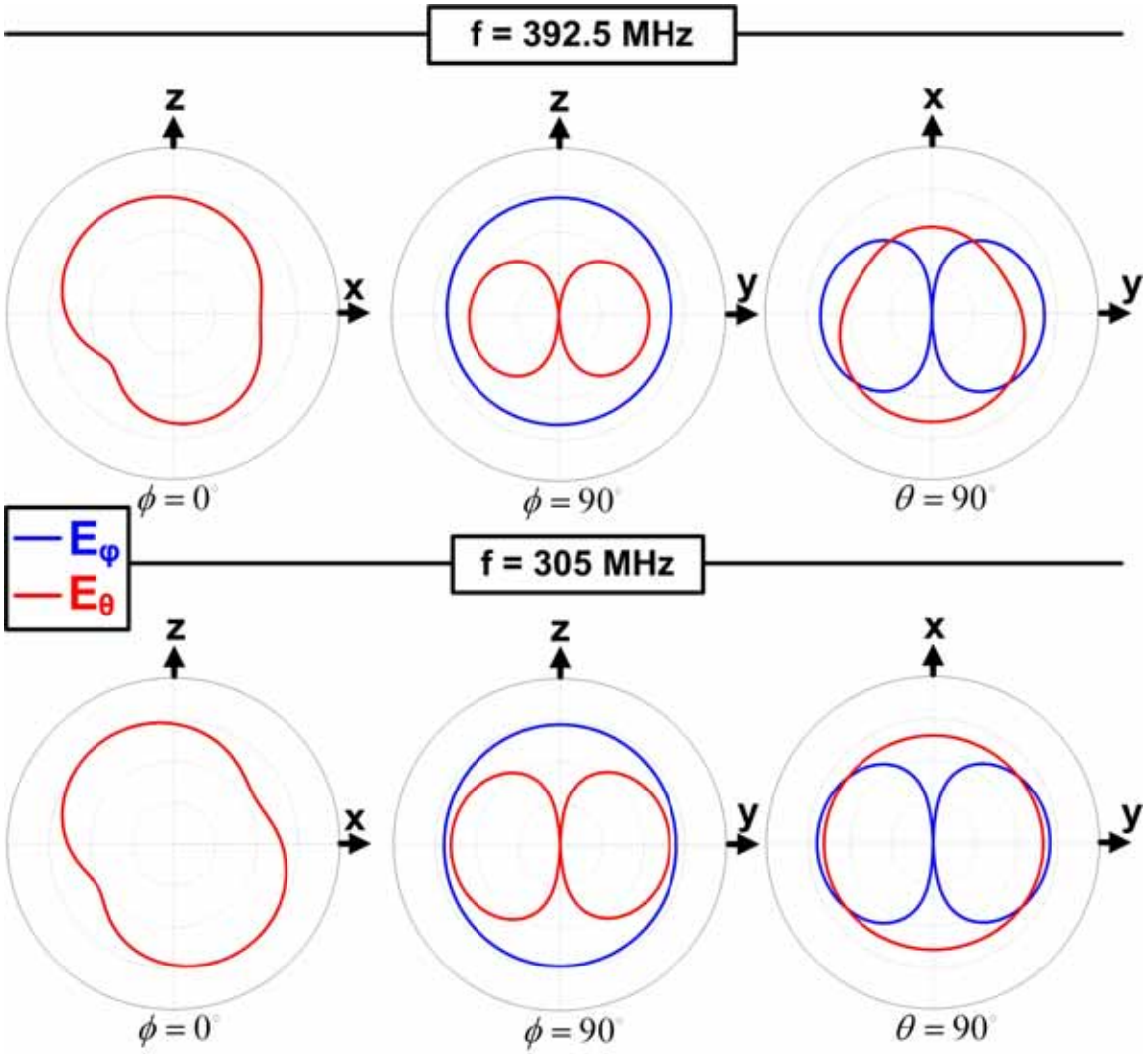

Fig. 40. Two Element Slotted *SIFA* - Radiated Fields. Radiation patterns in the three primary cut planes for the dual band *SIFA*, plotted over a minimum -30 dB, maximum 10 dB, with 10 dB divisions. The patterns in each band maintain their original characteristics in isolation from other elements

The two designs presented indicate that multiple elements provide significant gains in dual band and phased array operation; however, several design considerations, particularly coupling for the phased array design and operating frequency for the dual band design, need to be investigated more thoroughly.

C. Dielectric Coating and Biomedical Implantation

Although slot loading significantly reduces size while maintaining MICS band operation, the structure remains too large for ingestible biomedical applications. The dual L slotted *SIFA* is coated with high permittivity material to achieve further miniaturization. The coating also serves as a barrier between radiating elements and the body environment. The coating shields the antennas from caustic body fluids and the body from inorganic materials which comprise the antenna and sensor elements. A coating of permittivity $\varepsilon_r = 56$ was chosen for the coating, with this value representing the permittivity of the human body, averaged over the full range of human tissues. Table 8 presents a compilation of the electrical properties of several human tissues [64].

Table. 8. Electrical Properties of Biological Media

Tissue	Permittivity	Conductivity (S/m)
Bone	**13.1**	**0.09**
Fat	**11.6**	**0.08**
Skin	**46.7**	**0.69**
Muscle	**58.8**	**0.84**
Lungs	**54.6**	**0.68**
Heart	**66**	**0.97**
Liver	**51.2**	**0.65**
Stomach	**67.5**	**1**

After coating the antenna with high permittivity dielectric ($\varepsilon_r = 56$), the structure was scaled by a factor of 12 for operation at MICS band, resulting in a radius $R_o = 8.5$ mm. The design parameters were retuned, as shown in Table 9. The antenna geometry is identical to the larger dual L slot design, with the exception of a one millimeter thick dielectric coating. The design was initially matched at MICS band in a medium with the same permittivity as the coating, which represents the aggregate environment of the human body.

Table. 9. Miniaturized *SIFA* - Design Parameters

Parameter	Variable	Value
Outer Radius	R_o	**8.5 mm**
Inner Radius	R_i	**5 mm**
Coating Thickness	d	**1 mm**
Feed Angle	θ_f	**18°**
Slot Length Angle	θ_g	**2°**
Short Length Angle	θ_s	**2°**
Short Width Angle	φ_s	**50°**
Patch Width Angle	φ_w	**45°**
Slot Width Angle	θ_{ss}	**3°**
Slot Length Angle	φ_{ss}	**40°**
L-Slot Length Angle	θ_L	**30°**

Following coating and miniaturization, *SIFA* performance was simulated in various biological media to determine the effect of changes in the external environment on operating frequency and bandwidth. Four tissue samples - stomach, muscle, fat, and bone - were chosen to represent two limiting environments, with stomach and muscle representing the highest permittivity environment and fat and bone representing the lowest permittivity environment. Fig. 41 presents the VSWR and Smith data for the

miniaturized *SIFA* operating in stomach and muscle tissue. The *SIFA* operating frequency decreases slightly in both media because the tissue permittivity exceeds that of the coating. Thus, placing the *SIFA* in stomach or muscle effectively loads the antenna with a higher permittivity material and resonant frequency. The bandwidth increases due to losses in the environment. The VSWR 2:1 bandwidth contains the MICS band in both cases.

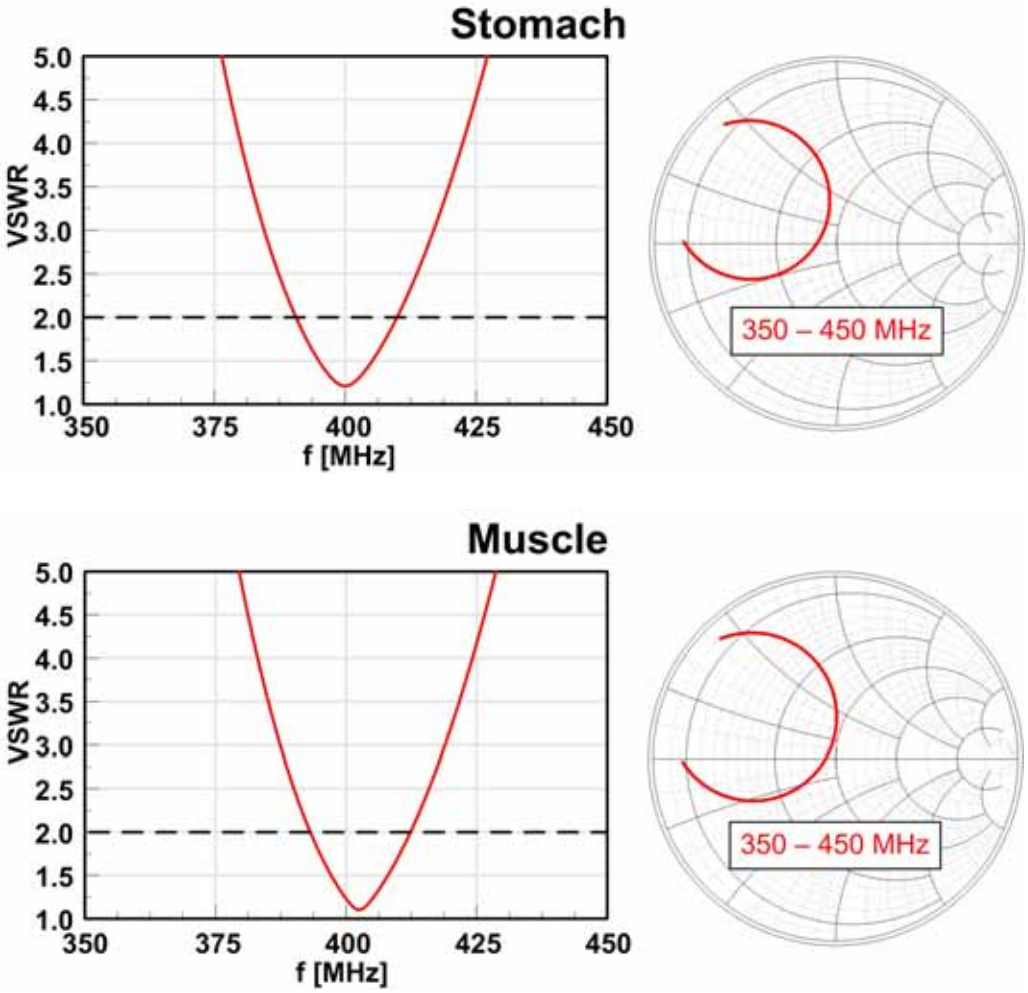

Fig. 41. Miniaturized *SIFA* - VSWR, Smith Response in Stomach & Muscle. The resonant frequency shifts slightly, and the bandwidth increases due to the lossy environment

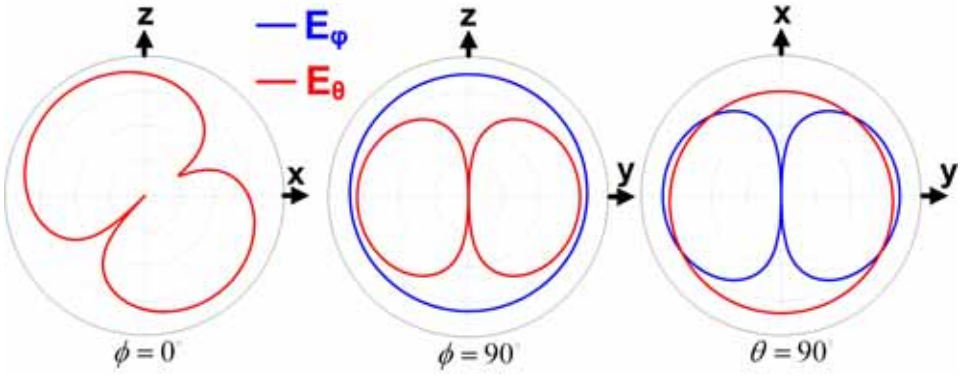

Fig. 42. Miniaturized *SIFA* - Radiated Fields in Stomach. Radiation patterns for the miniaturized *SIFA* in stomach tissue, plotted over a minimum -50 dB, maximum -10 dB, with 10 dB divisions. The radiation patterns behave similarly in other biological media

The radiation patterns for the miniaturized *SIFA* in stomach tissue, which can be seen in Fig. 42, mimic those of the original *SIFA*, with a 15.7 dB loss due to the conductive body environment. The antenna performs similarly in muscle. Fig. 43 presents the VSWR and Smith data for the miniaturized *SIFA* operating in fat and bone. The resonant frequency increases as the tissue permittivity decreases, in keeping with dielectric loading effects, until the antenna detunes completely out of the MICS band. The resonant frequency f_r = 423 MHz represents a 4.7 % increase relative to the original device operation at MICS band. The range of dielectric properties present in the human body presents a challenge to effective antenna design, since the antenna detunes as the external environment changes. The *SIFA* radiation patterns in bone and fat perform similarly to those in stomach and muscle.

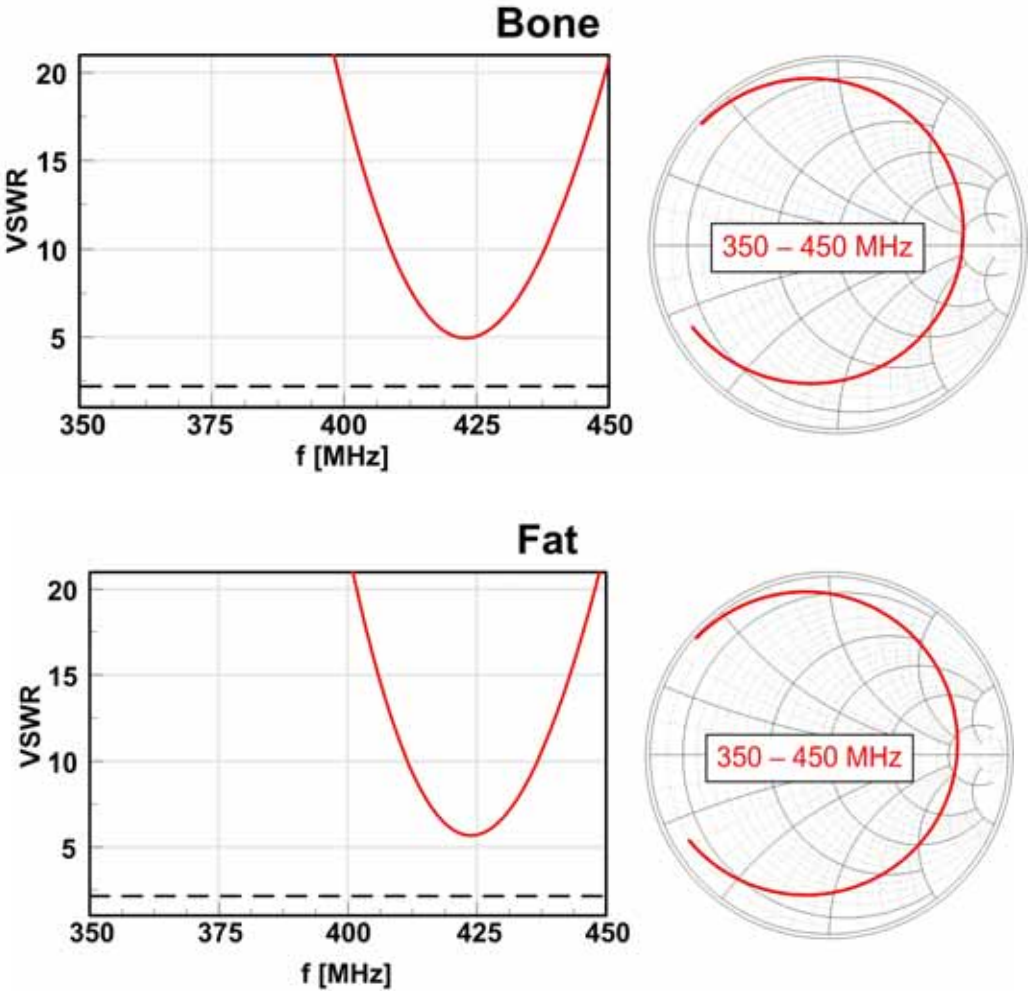

Fig. 43. Miniaturized *SIFA* - VSWR, Smith Response in Fat & Bone. The antenna detunes completely due to the change in external environment

Introducing loss in the *SIFA* coating provides a potential solution to antenna detuning in diverse environments. Since the miniaturized *SIFA* operates in highly lossy media, including a small loss in the coating could enhance the impedance match and expand bandwidth to contain the MICS band while contributing a small loss in the antenna gain. The decrease in antenna gain could potentially be offset by a decrease in reflected power (VSWR), resulting in a net increase in realized gain. Fig. 44 presents

the *SIFA* response to lossy coating in a fat or bone environment, with each curve on the Smith chart representing a variation in the coating loss tangent. Lossy dielectric coating allows matching in bone and fat; however, the resonant frequency f_r = 423 MHz remains well above MICS band. Nonetheless, the lossy design achieves a significant improvement over the original design by reducing the VSWR at MICS band from approximately 20:1 to 4:1. Further work on *SIFA* matching in ingestible environments will focus on determining the optimum coating permittivity and loss tangent for matching across the diverse range of biological media.

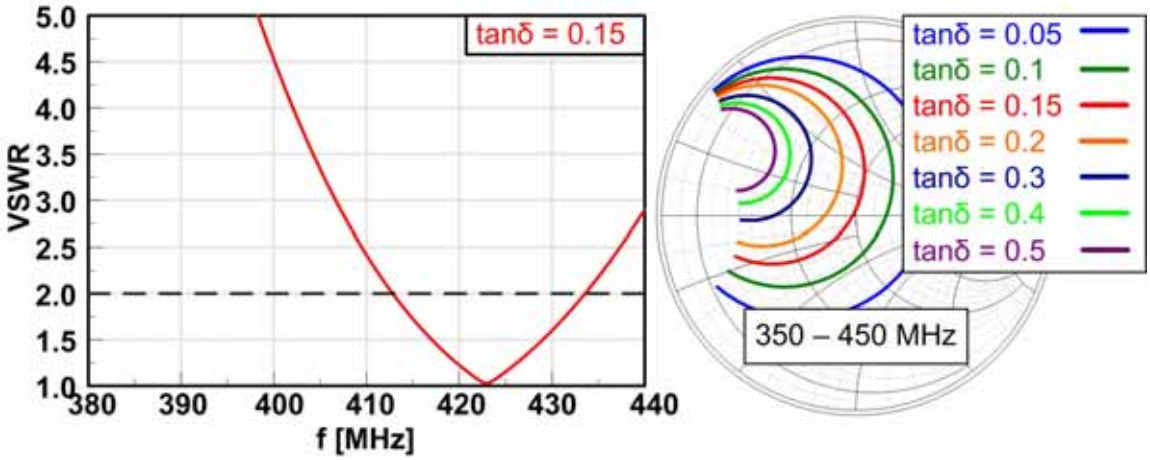

Fig. 44. Miniaturized SIFA - Effect of Lossy Coating in Fat & Bone. VSWR and Smith Response for the miniaturized *SIFA* coated with lossy material in fat and bone. Introducing loss achieves a match, but at a resonant frequency too high for operation in MICS band

CHAPTER VI

CONCLUSION

This work presents the use of advanced antenna integration and packaging techniques to analyze and design a Spherical Inverted-F Antenna, or *SIFA*. Measurement of a fabricated prototype agrees well with analytical and simulated results, and ongoing work promises a design space as diverse as that of planar microstrip technology. *SIFA* design draws on a well-established foundation of microstrip design techniques while exploiting the positive effects of conformal structures, most notably reduced size and improved omni-directionality. The initial analysis, simulation, and fabrication, as well as ongoing work in *SIFA* miniaturization and enhanced functionality, indicate the viability of the *SIFA* in a broad range of applications, including mobile, ad hoc, and reconfigurable sensor networks, microsatellite networks, and communication with ingested biomedical devices.

Preliminary work on slot loading, multiple antenna elements, and biomedical implantation indicate several directions for future work. Implementing slot loading in a fabricated prototype and verifying performance in a human body phantom would validate simulated results and confirm the potential for *SIFA* operation in the human body. Further work on slot loading, including U-slots for dual band operation and meander or serpentine designs for further miniaturization, could improve antenna characteristics while providing a baseline for comparison with planar implanted antennas [48, 64]. Introducing multiple elements on the *SIFA* surface could allow multi-band

operation for a single sensor; furthermore, multiple elements for phased array operation segues into research on pattern diversity for mobile, ad-hoc wireless networks. Multiple antenna systems could expand conformal design in the same way that array theory has expanded the application space for planar antennas. As the list of wireless applications stretches on, the fabrication difficulty becomes an issue. An investigation into fabrication techniques for conformal or curvilinear structures, such as stereolithography and lamination techniques, might streamline the fabrication process and strengthen the *SIFA*'s commercial viability.

Although the above areas focus on application, the development of more precise theoretical models could simplify the design process. Given the complexity of the small radiator in the presence of a spherical scattering object and the increasing demand for small conformal antennas, a great need exists to translate theory into closed-form design equations to assist the design engineer. A rigorous modification of the cavity model for conformal surfaces with a small radius of curvature, or the invention of a completely new model, could provide the basis for a holistic design process.

REFERENCES

[1] G. Marconi, "Wireless Telegraphy," *US Patent Office*, No. 786,132. 28 March 1905.

[2] V.O.K. Li, and X. Qiu, "Personal communication systems," *Proceedings of the IEEE*, vol. 83, no. 9, Sept. 1995, pp. 1210 – 1243.

[3] K.D. Katsibas, C.A. Balanis, P.A. Tirkas, and C.R. Bircher, "Folded loop antenna for mobile hand-held units," *IEEE Transactions on Antennas and Propagation*, vol. 46, no. 2, February 1998, pp. 260-266.

[4] B. Hicks, "Transforming avionics architectures to support network centric warfare," *in Proc. 23rd Digital Avionics Systems Conference*, vol. 2, 24-28 October 2004.

[5] W. Slelam, A.A. Mitkees, and M.M. Ibrahim, "Wideband planar phased array antenna at Ku frequency-band for synthetic aperture radars and radar-guided missiles tracking and detection," *in Proc. 2006 IEEE Conference on Radar*, 24-27 April 2006.

[6] H.S. Yoon, D.H. Lee, G. Lee, K.J. Kim, "A study on the information superiority of network centric warfare for future battlefield," *in Proc. 2008 International Conference on Information Science and Security*, 10-12 January 2008.

[7] V.P Hubenko, R.A. Raines, R.F. Mills, R.O. Baldwin, B.E. Mullins, et al, "Improving the global information grid's performance through satellite

communications enhancements," *IEEE Communications Magazine*, vol. 44, no. 11, November 2006, pp. 66-72.

[8] R. Gopal, S. Arnold, L. Orr, S. Ali, "Network centric satellite communication with IP networks based on regenerative satellite Mesh-A (RSM-A) Ka band technology," *in Proc. 2008 IEEE Military Communications Conference*, 16-19 November 2008, pp. 1-7.

[9] K.S. Low, W.N.N. Win, M.J. Er, "Wireless sensor networks for industrial environments," *Computational Intelligence for Modelling, Control and Automation and 2005 International Conference on Intelligent Agents, Web Technologies and Internet Commerce* , vol. 2, 28-30 November 2005, pp. 271-276.

[10] F. Salvadori, M. de Campos, R. de Figueiredo, C. Gehrke, C. Rech, et al, "Monitoring and diagnosis in industrial systems using wireless sensor networks," *in Proc. 2007 IEEE International Symposium on Intelligent Signal Processing*, 3-5 October 2007, pp. 1-6.

[11] A. Flaminni, P. Ferrari, D. Marioli, E. Sisinni, and A. Taroni, "Sensor networks for industrial applications," *in Proc. 2nd International Workshop on Advances in Sensors and Interfaces,* 26-27 June 2007, pp. 1-15.

[12] A. M Madni, "Smart configurable wireless sensors and actuators for industrial monitoring," *in Proc. 3rd International Symposium on Communications, Control and Signal Processing*, 12-14 March 2008, pp. 447-448.

[13] M. Bertocco, G. Gamba, A. Sona, and S. Vitturi, "Experimental characterization of wireless sensor networks for industrial applications," *IEEE Transactions on Instrumentation and Measurement*, vol. 57, no. 8, August 2008, pp. 1537-1546.

[14] A. Hierlemann, O. Brand, C. Hagleitner, and H. Baltes, "Microfabrication techniques for chemical/biosensors," *Proceedings of the IEEE*, vol. 91, no. 6, June 2003, pp. 839-863.

[15] W.J. Fleming, "Overview of automotive sensors," *IEEE Sensors Journal*, vol. 1, no. 4, December 2001, pp. 296-308.

[16] N.I. Maluf, G.T.A. Kovacs, D. Gee, "Recent advances in medical applications of MEMS," *WESCON 1996*, 22-24 October 1996, pp. 60-63.

[17] B. Mizaikoff, C. Kranz, L. Hvozdara, and M. Janotta, "Current applications and new trends in mid-infrared sensor technology and scanning probe sensors," *in Proc. First ISA/IEEE Sensors for Industry Conference*, 5-7 November 2001, pp. 208-213.

[18] D. Berdat, V. Sauvage, L. Bernau, D. Killis, and M.A.M. Gijs, "Biosensor for the detection of specific DNA sequences by impedance spectroscopy," *in Proc. Solid-State Sensors, Actuators and Microsystems Conference*, 10-14 June 2007, pp. 951-954.

[19] C. Moldovan, B. Kim, S. Raible, and V. Moagar, "Simulation and microfabrication of polysilicon structures used as mass sensitive sensors for gas detection," *in Proc. International Semiconductor Conference*, vol. 2, 10-14 October 2000, pp. 459-462.

[20] D. Liu, E. Flint, B. Gaucher, "Integrated laptop antennas – design and evaluation," *in Proc. 2002 IEEE Antennas and Propagation Society International Symposium*, vol. 4, 16-21 June 2002, pp. 56-59.

[21] S.-H. Wi, J.-S. Kim, N.-K. Kang, J.-C Kim, H.-G. Yang, et al, "Package-level integrated LTCC antenna for RF package application," *IEEE Transactions on Advanced Packaging*, vol. 30, no. 1, February 2007, pp. 132-141.

[22] K. Lim, A. Obatoyinbo, M. Davis, J. Laskar, R. Tummala, "Development of planar antennas in multi-layer packages for RF-system-on-a-package applications," *Electrical Performance of Electronic Packaging*, 29-31 October 2001, pp. 101-104.

[23] C.A. Balanis, *Antenna Theory: Analysis and Design*, 3rd Ed., New York: Wiley, 2004.

[24] F.T. Ulaby, *Fundamentals of Applied Electromagnetics*, 3rd Ed., New Jersey: Pearson Prentice Hall, 2004.

[25] K. Chang, *RF and Microwave Wireless Systems*, New York: Wiley, 2000.

[26] R.C. Hansen, "Fundamental limitations in antennas," *Proceedings of the IEEE*, vol. 69, no. 2, February 1981, pp.170-182.

[27] L.J. Chu, "Physical limitations of omnidirectional antennas," *Journal of Applied Physics*, vol. 19, December 1948, pp.1163-1175.

[28] Y.T. Lo, D. Solomon, W. Richards, "Theory and experiment on microstrip antennas," *IEEE Transactions on Antennas and Propagation*, vol. 27, no. 2, March 1979, pp. 137-145.

[29] W. Richards, Y.T. Low, D. Harrison, "An improved theory for microstrip antennas and applications," *IEEE Transactions on Antennas and Propagation*, vol. 29, no. 1, January 1981, pp. 38-46.

[30] K. Carver, J. Mink, "Microstrip antenna technology," *IEEE Transactions on Antennas and Propagation*, vol. 29, no. 1, Jan 1981, pp. 2-24.

[31] A. Derneryd, "A theoretical investigation of the rectangular microstrip antenna element," *IEEE Transactions on Antennas and Propagation*, vol. 26, no. 4, July 1978, pp. 532-535.

[32] S.A. Schelkunoff, "Some equivalence theorems of electromagnetics and their application to radiation problems," *Bell Sys. Tech. Journ.*, vol. 15, 1936, pp. 92-112.

[33] A. Derneryd, "Linearly polarized microstrip antennas," *IEEE Transactions on Antennas and Propagation*, vol. 24, no. 6, November 1976, pp. 846-851.

[34] H. Pues, A. van de Capelle, "Accurate transmission-line model for the rectangular microstrip antenna," *IEE Proceedings H - Microwaves, Optics, and Antennas*, vol. 131, no. 6, December 1984, pp. 334-340.

[35] E. Hammerstad, O. Jensen, "Accurate models for microstrip computer-aided design," *in Proc. IEEE MTT-S International Microwave Symposium*, Washington DC, 1980, pp. 407-409.

[36] M. Kirsching, R. H. Jansen, N.H.L. Koster, "Accurate model for open end effect of microstrip lines," *Electronics Letters*, vol. 17, no. 3, February 1981, pp. 123-125.

[37] R.F. Harrington, *Time Harmonic Electromagnetic Fields*, New York: IEEE Press, 2001.

[38] R.P. King, C.W. Harrison, and D.H. Denton, "Transmission-line missile antennas," *IRE Transactions on Antennas and Propagation*, January 1960. pp. 88-90.

[39] I.J. Bahl, P. Bhartia, *Microstrip Antennas*, Dedham, MA: Artech House, 1980.

[40] R. Waterhouse, "Small microstrip patch antenna," *Electronics Letters*, vol. 31, no. 8, 13 April 1995, pp. 604-605.

[41] K. Rambabu, M. Ramesh, A.T. Kalghatgi, "Design method for patch antennas short circuited at one end," *in Proc. 1997 Microwave Conference*, vol. 1, 2-5 December 1995, pp. 233-236.

[42] R.C. Johnson and H. Jasik, *Antenna Engineering Handbook*, New York: McGraw-Hill, 1984.

[43] T. Huynh and K.-F. Lee, "Single-layer single-patch wideband microstrip antenna," *Electronics Letters*, vol. 31, no. 16, 3 Aug. 1995, pp.1310-1312.

[44] M. Clenet and L. Shafai, "Multiple resonances and polarization of U-slot patch antenna," *Electronics Letters*, vol. 35, no. 2, 21 January 1999, pp. 101-103.

[45] P. Salonen, M. Keskilammi, M. Kivikoski, "Single-feed dual-band planar inverted-F antenna with U-shaped slot," *IEEE Transactions on Antennas and Propagation*, vol. 48, no. 8, August 2000, pp. 1262-1264.

[46] A. K. Shackelford, K.-F. Lee, and K.M. Luk, "Design of small-size wide-bandwidth microstrip-patch antennas," *IEEE Antennas and Propagation Magazine*, vol. 45, no. 1, February 2003, pp. 75-83.

[47] P. Salonen, M. Keskilammi, "Novel dual-band planar inverted-F antenna," *in Proc. 2000 Asia-Pacific Microwave Conference*, 3-6 December 2000, pp. 706-710.

[48] P. Soontornpit, C.M. Furse, Y.C. Chung, "Design of implantable microstrip antenna for communication with medical implants," *IEEE Transactions on Microwave Theory and Techniques*, vol. 52, no. 8, August 2004, pp. 1944-1951.

[49] H.Y. Wang, M.J. Lancaster, "Aperture-coupled thin-film superconducting meander antennas," *IEEE Transactions Antennas and Propagation*, vol. 47, no. 5, May 1999, pp. 829-836.

[50] C.R. Rowell, R.D. Murch, "A compact PIFA suitable for dual-frequency 900/1800-MHz operation," *IEEE Transactions on Antennas and Propagation*, vol. 46, no. 4, April 1998, pp. 596-598.

[51] V. Palanisamy, R. Garg, "Rectangular ring and H-shaped microstrip antennas: alternatives to rectangular patch antenna," *Electronics Letters*, vol. 21, no. 19, 12 September 1985, pp. 874-876.

[52] K.L. Lau, K.M. Luk, K.C. Kong, "Wideband folded L-slot shorted patch antenna," *in Proc. 2007 IEEE Antennas and Propagation International Symposium*, 9-15 June 2007, pp. 6019 - 6022.

[53] Y. Hwang, Y.P. Zhang, T.K.C. Lo, K.M. Luk, and E.K.N. Yung, "Miniaturization on planar antennas with very high permittivity materials," *in Proc. 1997 Asia-Pacific Microwave Conference*, vol. 1, 2-5 December 1997, pp. 217-220.

[54] Y. Hwang, Y.P. Zhang, G.X. Zheng, and T.K.C. Lo, "Planar inverted-F antenna loaded with high permittivity material," *Electronics Letters*, vol. 31, 1995, pp. 1710-1712.

[55] R. Munson, "Conformal microstrip antennas and microstrip phased arrays," *IEEE Transactions on Antennas and Propagation*, vol. 22, no. 1, January 1974, pp. 74-78.

[56] K. Luk, K.-F. Lee, J.S. Dahele, "Analysis of the cylindrical-rectangular patch antenna," *IEEE Transactions on Antennas and Propagation*, vol. 37, no. 2, February 1989, pp. 143-147.

[57] B.R. Piper, M.E. Bialkowski, "Modelling the effect of 3D conformity on single and multi-band patch antennas," *in Proc. 2003 IEEE Antennas and Propagation Society International Symposium*, vol. 3, 22-27 June 2003, pp. 116-119.

[58] K. Wu, J. Kauffman, "Radiation pattern computations for spherical-rectangular microstrip antennas," *in Proc. 1983 Antennas and Propagation Society International Symposium*, vol. 21, May 1983, pp. 43-46.

[59] C. Krowne, "Cylindrical-rectangular microstrip antenna," *IEEE Transactions on Antennas and Propagation*, vol. 31, no. 1, January 1983, pp. 194-199.

[60] J.S. Dahele, R.J. Mitchell, K.M. Luk, and K.F. Lee, "Effect of curvature on characteristics of rectangular patch antenna," *Electronics Letters*, vol. 23, no. 14, 2 July 1987, pp. 748-749.

[61] L.C. Kempel, J.L. Volakis, R. J. Silva, "Radiation by cavity-backed antennas on a circular cylinder," *IEE Proceedings - Microwaves, Antennas, and Propagation*, vol. 142, no. 3, June 1995, pp. 233-239.

[62] J.T. Aberle and F. Zavosh, "Analysis of probe-fed circular microstrip patches backed by circular cavities," *Electromagnetics*, vol. 14, 1994, pp. 239-258.

[63] S. Koulouridis, G. Kiziltas, Y. Zhou, D.J. Hansford, and J. L. Volakis, "Polymer-ceramic composites for microwave applications: fabrication and performance assessment," *IEEE Transactions on Microwave Theory and Techniques*, vol. 54, no. 12, December 2006, pp. 4202 - 4208.

[64] J. Kim, R. Y. Rahmat-Samii, "Implanted antennas inside a human body: simulations, designs, and characterizations," *IEEE Transactions on Microwave Theory and Techniques*, vol. 52, no. 8, August 2004, pp. 1934-1943.

APPENDIX A

DERIVATION OF SIDE SLOT CONDUCTANCE G_{ss}

First consider the distribution of tangential electric field in the aperture, as shown in Fig. 45.

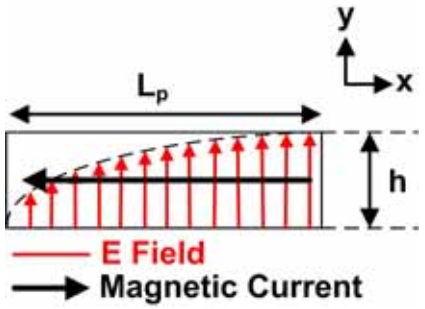

Fig. 45. Side Slot - Tangential E-field Distribution. Electric field distribution and equivalent magnetic current for the *SIFA* side slot. The slot curvature has been approximated by equivalent rectangular dimensions

The tangential electric field can be written as:

$$\vec{E}_a = \hat{a}_y E_o \sin\left(\frac{\pi x'}{2L_p}\right) \tag{13}$$

From which the equivalent magnetic current can be determined as:

$$\vec{M}_s = -2\hat{n} \times \vec{E}_a = \hat{a}_x 2E_o \sin\left(\frac{\pi x'}{2L_p}\right) \tag{14}$$

The electric vector potential can be determined from the magnetic current as:

$$\vec{F} = \frac{\varepsilon}{4\pi} \iint_{S'} \vec{M}_s \frac{e^{-jkR}}{R} ds' \tag{15}$$

Simplifying the electric vector potential in terms of θ and φ components gives:

$$\begin{aligned} F_\theta &= \frac{\varepsilon e^{-jkr}}{4\pi r} 2E_o \cos(\theta)\cos(\phi) I \\ F_\phi &= -\frac{\varepsilon e^{-jkr}}{4\pi r} 2E_o \sin(\phi) I \end{aligned} \tag{16}$$

Where the integral I is:

$$I = \int_{0}^{L_p} \int_{-\frac{h}{2}}^{\frac{h}{2}} e^{jky'\sin(\theta)\sin(\phi)} \sin\left(\frac{\pi x'}{2L_p}\right) e^{jkx'\sin(\theta)\sin(\phi)} dy'dx' \tag{17}$$

The electric field in the far field can be determined from the electric vector potential as:

$$\begin{aligned} E_\theta &= -j\omega\eta F_\phi \\ E_\phi &= j\omega\eta F_\theta \end{aligned} \tag{18}$$

From which the radiated power from the slot is:

$$P = \frac{1}{\eta} \oiint_{\theta,\phi} \left(\left|E_\phi\right|^2 + \left|E_\theta\right|^2 \right) r^2 d\theta d\phi \tag{19}$$

and the slot conductance:

$$\begin{aligned} G_{ss} &= \frac{2P}{\left|V_o\right|^2} \\ V_o &= hE_o \end{aligned} \tag{20}$$

Returning to the integral I, it can be evaluated as:

$$\begin{aligned} I &= \frac{h}{2j} \frac{\sin(Y)}{Y} \left[\frac{je^{jL_p k\sin(\theta)\cos(\phi)} - 1}{k\sin(\theta)\cos(\phi) + \frac{\pi}{2L_p}} + \frac{je^{jL_p k\sin(\theta)\cos(\phi)} + 1}{k\sin(\theta)\cos(\phi) - \frac{\pi}{2L_p}} \right] \\ Y &= \frac{kh}{2}\sin(\theta)\sin(\phi) \end{aligned} \tag{21}$$

which is a function of spatial variables θ, φ, slot dimensions h, L_p, and propagation constant k. Thus, having solved for I, the electric vector potential, electric field, power radiated, and slot conductance can be calculated as outlined above:

$$I \rightarrow F_{\theta,\phi} \rightarrow E_{\theta,\phi} \rightarrow P \rightarrow G_{ss} \tag{22}$$

The integral for P over spatial variables θ and φ is performed numerically in Matlab, as shown in Appendix B. Thus the slot conductance G_{ss} can be determined as a function of frequency for various SIFA design parameters.

APPENDIX B

MATLAB CODE - SIDE SLOT CONDUCTANCE G_{ss}

```
function [Gss]= ssg(W,h,k)

% This code calculates the conductance of a rectangular aperture with a
% half-sinusoidal E-field distribution (i.e. the side slot of
% a PIFA or SUFA), for inclusion in a TL model. This code draws heavily
% on the aperture theory analysis from Balanis [23] Chapter 12. This
% code was written in Matlab version R2007a.

% Define constants.
eta=120*pi; % Free space impedance
dphi=pi/90; % Integration step in phi
dtheta=dphi; % Integration step in theta
theta=0:dtheta:pi; % Over half space
phi=0:dphi:2*pi;
[T,P]=meshgrid(theta,phi); % Spatial matrices covering half space

% Calculate intermediate variables
X1=k*sin(T).*cos(P)+pi/(2*W);
X2=X1-pi/W;
Y=k*h/2*sin(T).*sin(P);

% Evaluate integral formulation in electric vector potential.
A=1/2*(sinc(Y)).*(((exp(j*W*X1)-1)./X1)+((exp(j*W*X2)-1)./X2));

% Calculate E-fields from electric vector potentials.
Ltheta=2*cos(T).*cos(P).*A;
Lphi=2*sin(P).*A;
Etheta=k/(4*pi)*Lphi;
Ephi=k/(4*pi)*Ltheta;
AET=(abs(Etheta)).^2;
AEP=(abs(Ephi)).^2;

% Integrate normalized power over half space and thus slot conductance.
Power=1/(2*eta)*(sum(sum(AET.*sin(T))*dphi)*dtheta...
    +sum(sum(AET.*sin(T))*dphi)*dtheta);
Gss=2*Power;
```

APPENDIX C

MATLAB CODE - ANALYTICAL MODEL

```
clear all; close all; clc;

% This code calculates SIFA performance - input impedance, reflection
% coefficient, and VSWR - from physical design parameters. This
% code was written in Matlab version R2007a.

% Define universal variables
c=3e8; % Speed of light
fr=404e6; % Desired resonant frequency
lambdar=c/fr; % Resonant free space wavelength
kr=2*pi/lambdar; % Resonant propagation constant
Zline=50; % Line impedance to match to
eta=120*pi; % Characteristic impedance of free space
d=0.615e-3; % Probe diameter

% Define SIFA design parameters in angular form.
Ro=101.6e-3; % SIFA outer radius
Ri=76.2e-3; % SIFA inner radius
thetag=11; % Radiating gap in degrees
thetas=11; % Short length in degrees
phis=22; % Short width in degrees
phip=90; % Patch width in degrees
thetaf=9; % Feed location in degrees

% Convert angular parameters to arc lengths and calculate equivalent
% patch parameters
epsr=1; % Substrate permittivity
h=Ro-Ri; % Substrate height
Wp=2*pi*Ro*phip/360; % Patch Width
Ws=2*pi*Ro*phis/360; % Short Width
Lg=2*pi*Ro*thetag/360; % Radiating Gap Length
Ls=2*pi*Ro*thetas/360; % Short Length
Lp=(pi/2*Ro-Lg-Ls)*cos(phip/2*pi/180); % Patch Length
Lf=2*pi*Ro*thetaf/360; % Feed position
Lpc=(pi/2*Ro-Lg-Ls); % Patch length along center of patch width

% Calculate probe inductance.
x=sqrt(1+(2*d/(2*h))^2);
L=2*h*100*(log((h/d)*(1+x))-x+d/(h))*1e-9;

% Calculate effective permittivity for patch and short.
eep=(epsr+1)/2+...
    (epsr-1)/2*(1+12*h/Wp)^(-1/2); % Effective patch permittivity;
ees=(epsr+1)/2+...
    (epsr-1)/2*(1+12*h/Ws)^(-1/2); % Effective short permittivity

% Calculate patch and short characteristic impedance for use in TL
% model.
```

```
Zp=120*pi/(sqrt(eep)*(Wp/h+1.393+0.667*log(Wp/h+1.444)));
Zs=120*pi/(sqrt(ees)*(Ws/h+1.393+0.667*log(Ws/h+1.444)));
Yp=Zp^(-1); Ys=Zs^(-1); % Conversion to admittance

% Effective length extension due to slots and shorting, from
% Balanis[23]
dL=0.412*h*(eep+.3)/(eep-.258)*(Wp/h+0.262)/(Wp/h+0.813);
Lpeff=Lp+(Wp-Ws)/2+dL;

% Define frequency range and step. Slot admittances and TL parameters
% are calculated as a function of frequency.
deltaf=1e6;
fll=200e6;
ful=600e6;

for f=fll:deltaf:ful
    freq((f-fll)/deltaf+1)=f; % Create frequency vector for plots

    lambda=c/f; % Free space wavelength
    k=2*pi/lambda; % Free space propagation constant
    leffp=lambda/sqrt(eep); % effective wavelength in patch
    kep=2*pi/leffp; % effective prop constant in patch
    leffs=lambda/sqrt(ees); % effective wavelength in patch
    kes=2*pi/leffs; % effective prop constant in patch

% Calculate radiating slot admittance
    G1=Wp/(120*lambda)*(1-1/24*(k*h)^2); % Slot self conductance
    B1=Wp/(120*lambda)*(1-0.636*log(k*h)); % Slot self susceptance
    Yslot=G1+j*1*B1; % Slot self admittance
    Gss=ssg(Lp,h,k); % Side slot conductance

% Calculate probe reactance
    Xf=2*pi*f*L;
% Calculate input Z as a function of frequency.
    L1=Lf; L2=Lpeff-Lf-Ls; % Length on each side of feed
    Zls=j*Zs*tan(kes*Ls); Yls=Zls^(-1); % Input Z/Y of short
    Yin1=Yp*(Yls+j*Yp*tan(kep*L1))/(Yp+j*Yls*tan(kep*L1)); % Y1
    Yin2=Yp*(Yslot+j*Yp*tan(kep*L2))/(Yp+j*Yslot*tan(kep*L2)); % Y2

% Calculate total Y from short (Yin1), primary radiating slot (Yin2)
% and side slots (Gss)
    Yinp=Yin1+Yin2+2*Gss;
    Zinp=1/Yinp; % Total Z

% Put data into vector form for plotting. Include probe inductance in
% impedance.
    Yin((f-fll)/deltaf+1)=Yinp;
    Xfv((f-fll)/deltaf+1)=Xf;
    Zin((f-fll)/deltaf+1)=Zinp+j*Xf;
    Yside((f-fll)/deltaf+1)=Gss;
    Slot((f-fll)/deltaf+1)=Yslot;
end
```

```
% Calculate reflection coefficient, VSWR and prepare data for export.
Gammain=(Zin-Zline)./(Zin+Zline);
VSWR=(1+abs(Gammain))./(1-abs(Gammain));
R=real(conj(Zin'));
I=imag(conj(Zin'));
VSWR2=conj(VSWR');
S11R=real(conj(Gammain'));
S11I=imag(conj(Gammain'));

% Plot VSWR
figure(1); hold on;
plot(freq, VSWR);
xlabel('Frequency'); xlim([0.75*fr 1.25*fr])
ylabel('VSWR'); ylim([1 5])
title('VSWR vs. Frequency','FontSize',12)

% Plot input resistance
figure(2); hold on;
plot(freq, real(Zin))
xlabel('Frequency')
ylabel('Real Zin')
title('Real Zin vs. Frequency','FontSize',12)

% Plot input reactance
figure(3); hold on;
plot(freq, imag(Zin))
xlabel('Frequency'); xlim([fll ful])
ylabel('Imag Zin')
title('Imaginary Zin vs. Frequency','FontSize',12)

% Plot side slot conductance vs. frequency
figure(4)
plot(freq, 1./Yside)
xlabel('Frequency')
ylabel('Side Slot R')
title('Side Slot Resistance vs. Frequency','FontSize',12)

% Plot primary slot conductance vs. frequency
figure(5)
plot(freq, real(1./Slot))
xlabel('Frequency')
ylabel('Primary Slot R')
title('Slot Resistance vs. Frequency','FontSize',12)
```

VITA

Jacob Jeremiah McDonald
mcdonald.jacob@gmail.com

1201 Harvey Road, Apt. 91
College Station, TX 77840

Education

Institution	Major, GPA	Degree, Year
Texas A&M University College Station, TX	Electrical Engineering 4.0/4.0	B.S., 2007
Texas A&M University College Station, TX	Electrical Engineering 3.81/4.0	M.S., 2009

Research & Work Experience

- Teaching Assistant, Electromagnetics and Microwave Laboratory, ECEN Department, Texas A&M University, College Station, TX, Fall 2008 - Spring 2009
- Electrical Engineering Intern, Sandia National Laboratories, Synthetic Aperture Radar Group, Albuquerque, NM, May 2007 to August 2007, May 2008 to August 2008
- Research Assistant, Electromagnetics and Microwave Laboratory, ECEN Department, Texas A&M University, College Station, TX, Fall 2007 - Spring 2008
- Electrical Engineering Intern, Raytheon Company, Phased Array Group - Advanced Products Center, McKinney, TX, May 2006 - August 2006.

Publications and Conferences

[1] J.J. McDonald and G.H. Huff, "Microfluidic Reconfiguration Mechanisms for Dielectric Resonator Antennas," *in proc. 2008 URSI General Assembly*, 9 - 16 Aug. 2008.

[2] G.H. Huff and J.J. McDonald "Design and Packaging of A Spherical Inverted-F Antenna (SIFA) for Biomedical Applications," *in proc. 2007 IEEE Ant. Prop. Int. Symp.*, 5-12 July 2008.

Awards and Honors

- Fouraker-Ebsenberger Fellow, Department of Electrical and Computer Engineering, Texas A&M University, Fall 2007 - Spring 2008
- University Honors, Texas A&M University
- Foundation Honors, Texas A&M University
- University Undergraduate Research Fellow, Texas A&M Honors Program, Fall 2006 - Spring 2007
- Engineering Scholar, Dwight Look College of Engineering, Texas A&M University